

# SPECDis: Value added distance catalogue for 4 million stars from DESI Year-1 data

Songting Li,<sup>1,2,3\*</sup> Wenting Wang,<sup>1,2,3†</sup> Sergey E. Kposov,<sup>4,5‡</sup> Ting S. Li,<sup>6</sup> Youjia Wu,<sup>7,8</sup> Monica Valluri,<sup>7</sup> § Joan Najita,<sup>9</sup> Carlos Allende Prieto,<sup>10,11</sup> Amanda Byström,<sup>4</sup> Christopher J. Manser,<sup>12</sup> Jiaxin Han,<sup>1,2,3</sup> Carles G. Palau,<sup>1,2,3</sup> Hao Yang,<sup>13,1,2,3</sup> Andrew P. Cooper,<sup>14,15</sup> Namitha Kizhuprakkat,<sup>14</sup> Alexander H. Riley,<sup>16</sup> Jessica Nicole Aguilar,<sup>17</sup> Steven Ahlen,<sup>18</sup> David Bianchi,<sup>19,20</sup> David Brooks,<sup>21</sup> Todd Claybaugh,<sup>17</sup> Axel de la Macorra,<sup>22</sup> John Della Costa,<sup>23,24</sup> Arjun Dey,<sup>24</sup> Peter Doel,<sup>21</sup> Jaime E. Forero-Romero,<sup>25,26</sup> Enrique Gaztañaga,<sup>27,28</sup> Satya Gontcho A Gontcho,<sup>17</sup> Gaston Gutierrez,<sup>29</sup> Klaus Honscheid,<sup>30,31,32</sup> Mustapha Ishak,<sup>33</sup> Stephanie Juneau,<sup>24</sup> Robert Kehoe,<sup>34</sup> Theodore Kisner,<sup>17</sup> Martin Landriau,<sup>17</sup> Laurent Le Guillou,<sup>35</sup> Michael Levi,<sup>17</sup> Marc Manera,<sup>36,37</sup> Aaron Meisner,<sup>24</sup> Ramon Miquel,<sup>37,38</sup> John Moustakas,<sup>39</sup> Nathalie Palanque-Delabrouille,<sup>17,40</sup> Will Percival,<sup>41,42,43</sup> Claire Poppett,<sup>17,44,45</sup> Francisco Prada,<sup>46</sup> Ignasi Pérez-Ràfols,<sup>47</sup> Graziano Rossi,<sup>48</sup> Eusebio Sanchez,<sup>49</sup> David Schlegel,<sup>17</sup> Michael Schubnell,<sup>7,50</sup> Hee-Jong Seo,<sup>51</sup> Joseph Harry Silber,<sup>17</sup> David Sprayberry,<sup>24</sup> Gregory Tarlé,<sup>50</sup> Benjamin Alan Weaver,<sup>24</sup> Rongpu Zhou,<sup>17</sup> Hu Zou<sup>52</sup>

*Affiliations are listed at the end of the paper.*

Accepted XXX. Received YYY; in original form ZZZ

## ABSTRACT

We present the SPECDis value added stellar distance catalogue accompanying DESI DR1. SPECDis trains a feed-forward Neural Network (NN) on a large sample of stars with *Gaia* parallaxes, but without applying selections on parallax error or signal-to-noise (S/N) of the stellar spectra. We incorporate parallax error into the loss function for training. This approach ensures the training sample not suffering from biases. Moreover, SPECDis predicts the reciprocal of the square root of luminosity, which is linearly proportional to parallax and helps to avoid excluding negative parallaxes. To enhance the precision of distance predictions, we employ Principal Component Analysis (PCA) to reduce the noise and dimensionality of stellar spectra. Validated by independent external samples of member stars with precise distances from globular clusters, dwarf galaxies, and stellar streams, combined with BHB stars, we demonstrate that our distance measurements show no significant bias up to 100 kpc, and are much more precise than *Gaia* parallax beyond 7 kpc. The median distance uncertainties are 23%, 19%, 11% and 7% for  $S/N < 20$ ,  $20 \leq S/N < 60$ ,  $60 \leq S/N < 100$  and  $S/N \geq 100$ . Selecting stars with  $\log g < 3.8$  and distance uncertainties smaller than 25%, we have more than 74,000 giant candidates within 50 kpc to the Galactic center and 1,500 candidates beyond this distance. Additionally, we develop a Gaussian mixture model to identify binaries by modeling the discrepancy between the NN-predicted and the geometric absolute magnitudes from *Gaia* parallaxes. We identify 120,000 possible binaries, and discover that the binary fraction increases with [Fe/H] and  $\log g$  and declines with  $[\alpha/\text{Fe}]$  and  $T_{\text{eff}}$ , indicating stars with low Fe and high  $\alpha$ , which form early, may have experienced more encounters and tidal effects to disrupt binaries. Our final catalogue provides distances and distance uncertainties for >4 million stars, offering a valuable resource for Galactic astronomy.

**Key words:** methods: data analysis – Milky Way: stars – Milky Way: stellar parameter

## 1 INTRODUCTION

Our Milky Way (MW) Galaxy is an ideal laboratory to test the physics of galaxy formation and the underlying cosmology, because individ-

ual stars in the MW can be resolved by the observers. Various types of information can be extracted from the phase-space distribution of individual stars in the Galaxy, and from its surrounding globular clusters (GCs), satellite galaxies and stellar streams, which enables us to probe the spatial and kinematical structures of the MW disk, bulge, and halo, to infer the assembly history of the MW (galactic archaeology), and construct dynamical models to constrain the nature of the host dark matter halo of our MW. In particular, full 6-

\* songtingli@sju.edu.cn

† Corresponding Author: wenting.wang@sju.edu.cn

‡ Sergey.Kposov@ed.ac.uk

§ mvalluri@umich.edu

dimensional phase-space information, without missing dimensions, is critical for scientific inferences.

Among the 6-dimensional phase-space information, distances to individual stars can be measured in several different ways. The approaches include, for example, measuring the parallax of individual stars, the usage of the period luminosity relation for RR Lyrae and Cepheids (e.g. [Hernitschek et al. 2017](#); [Clementini et al. 2019](#)), photometric distances to infer the luminosity from stellar colour (e.g. [Jurić et al. 2008](#); [Ivezić et al. 2008](#); [Huang et al. 2023](#)), and spectrophotometric distance when stellar atmospheric parameters and distances can be measured together from stellar spectra and photometry (e.g. [Xue et al. 2014](#); [Hogg et al. 2019](#); [Xiang et al. 2021](#); [Wang et al. 2022](#); [Zhang et al. 2024](#)). Among all the different methods, the geometric parallax measurements have been revolutionized by *Gaia* ([Gaia Collaboration et al. 2016](#)), but *Gaia* does not deliver precise parallaxes at the faint end ( $G > 17$ ) ([Lindgren et al. 2021](#)), out to large distances ( $> \sim 5$  kpc) or in crowded regions, and the errors also correlate with proper motion errors. Distances measured for variable stars are relatively accurate, but are not applicable to main sequence stars or giants which contribute the majority of stars. The photometric distance measurements of inferring the luminosity from stellar colour are known to suffer from errors of several tens of percent, and may be challenging for hot stars with less colour variation beyond the Rayleigh-Jeans tail. Spectrophotometric distance measurements combine spectroscopy and photometry, with the stellar spectra containing far more information than pure photometric colours, which can provide more precise predictions of the luminosity and distance. The quoted errors in the literature range from about  $\sim 10\%$  to  $20\text{--}30\%$ , depending on the spectral type of stars, the signal-to-noise ratio and resolution of the spectrum, and the methodology.

There are several different ways to perform the spectrophotometric distance measurements. One method involves deriving stellar parameters, and the absolute magnitudes (and hence distances) can be inferred through, for example, matching to stellar isochrones (e.g. [Carlin et al. 2015](#); [Wang et al. 2016](#); [Queiroz et al. 2020](#)) or through other probabilistic models (e.g. [Coronado et al. 2018](#)). To derive the stellar parameters, physical spectral models are adopted to fit to the observed data spectra.

Machine learning or deep learning approaches ([Goodfellow et al. 2016](#)) are extensively utilized to derive stellar parameters and absolute magnitudes, hence distances, from median-to-low-resolution spectra in a data-driven manner (e.g. [Xiang et al. 2017](#); [Hogg et al. 2019](#); [Xiang et al. 2021](#); [Green et al. 2021](#); [Wang et al. 2022](#)). These methods predict the stellar parameters and absolute magnitudes from the stellar spectra and photometry, by learning a model using a sample of stars with more accurate distance and stellar parameter measurements from, e.g., precise *Gaia* parallax and other independent, higher-resolution surveys with more accurate stellar parameter estimates.

More recently, the Payne method ([Ting et al. 2019](#); [Xiang et al. 2019, 2022](#)) has been developed and is regarded by the authors as a data-driven plus model-driven hybrid method. It adopts machine learning to build a forward model that predicts both the stellar spectral flux and gradients from a large number of stellar parameters, based on physical stellar atmospheric models or more precise measurements based on higher resolution spectroscopic survey data. The differentiable stellar spectra are fitted to the observed stellar spectra. The Payne method has recently been applied by [Zhang et al. \(2024\)](#) to the early survey data release of the Dark Energy Spectroscopic Instrument (DESI).

DESI is one of the foremost multi-object spectrographs for wide-field surveys ([Levi et al. 2013](#); [DESI Collaboration et al. 2016a,b](#);

[Silber et al. 2022](#); [Schlafly et al. 2023](#); [DESI Collaboration et al. 2024g](#)). The main science goal of DESI is to achieve the most precise constraint on the expansion history of the Universe to date with baryon acoustic oscillations (BAO) and other methods ([Levi et al. 2013](#)). For the goal, DESI observes four classes of galactic targets including the Bright Galaxy Survey targets (BGS; [Hahn & DESI Team 2022](#)), luminous red galaxies (LRG; [Zhou et al. 2023a](#)), emission line galaxies (ELG; [Raichoor et al. 2023](#)) and quasars ([Chaussidon et al. 2023](#)).

So far DESI has achieved many important science results ([DESI Collaboration et al. 2022](#)), including BAO signal from galaxies and Lyman alpha forest ([DESI Collaboration et al. 2024a,b](#)), full-shape galaxy clustering ([DESI Collaboration et al. 2024e](#)), two-point clustering statistics ([DESI Collaboration et al. 2024d](#)) and cosmological constraints ([DESI Collaboration et al. 2024c,f](#))<sup>1</sup>

In addition to extra-galactic observations, DESI also performs the so far largest survey for stars within our Galaxy. A great numbers of stellar spectra is being cumulated to better understand our own Galaxy and its dark matter halo through stellar kinematics. The Year-1 data already has more than 4 million stellar spectra. Accompanying the Year-1 observation, we adopt a data-driven approach to measure the distances of stars from the Year-1 data of the DESI MW Survey (MWS; [Cooper et al. 2023](#)) in this paper. Our attempt is among the various DESI MWS approaches aimed at providing distance measurements for main sequence and giant stars observed by DESI. Our stellar distance catalogue (SPECDIS) is published as one of the Value Added catalogues (VAC) of DESI DR1.

Similar to many previous data-driven approaches, in this work we utilize a feed-forward multilayer perceptron neural network to predict a quantity constructed from *Gaia* *G*-band apparent magnitude and parallax of *Gaia* data release 3 (DR3), that is then used to predict the distance of each star. There are quite a few key improvements in our approach. First of all, we are not directly predicting the absolute magnitudes, but instead we construct a quantity that is the reciprocal of the square root of luminosity, which is linearly proportional to parallax. This helps to avoid the necessity of excluding negative parallaxes. Moreover, we do not include any cuts on parallax error in the training sample, to avoid biasing the training sample and include any possible selection effects. Instead, we utilize nearly all DESI-observed stars with *Gaia* parallaxes, regardless of their precision, and we include the parallax measurement uncertainties upon constructing our loss function adopted to optimize the network, so that the neural network can recognize the parallax errors upon modeling. Additionally, a major difference in our approach compared to many previous studies is that we adopt PCA to decrease the noise and the dimensionality of the DESI stellar spectra. Instead of training using the spectra directly, we utilize the coefficients of the few major principal components denoised from the spectra for training.

Our validation of the test sample indicates that the precision of distance measurements is approximately  $10\%$  for the high signal-to-noise subset ( $S/N > 100$ ). Furthermore, we conducted an external validation of our distance estimates using member stars from globular clusters, dwarf galaxies, and the Sagittarius stellar stream, which have precise distance measurements from other methods and can thus serve as a reference. This external validation process shows that our distance measurements exhibit no significant bias up to 100 kpc. Based on our distance measurements, we have also proposed a model

<sup>1</sup> [DESI Collaboration et al. \(2022, 2024g,h,d,a,b,e,c,f\)](#) are DESI Collaboration Key Papers.

to distinguish binary stars from single stars, and have identified a population of 120,000 candidate binary systems.

This paper is organized as follows: Section 2 gives an overview of the data from the DESI MWS, including the construction of the total sample, the external validation sample and our initial processing and preparation of the stellar spectra. Section 3 introduces the methodology of this work. Section 4 describes the main results of our measured distances and precision validation. Section 5 offers further discussion on how to identify binary stars and some binary fraction statistics. We summarize our findings in Section 6.

## 2 DATA

### 2.1 The DESI Milky Way Survey

DESI is one of the foremost multi-object spectrograph operating at Kitt Peak National Observatory (Levi et al. 2013; DESI Collaboration et al. 2016a,b, 2022, 2024h). It features 5,000 fibers, that connect to 3-arm spectrographs (*B*, *R* and *Z*-arms), altogether span the rest-frame wavelength range of 3,600–9,824 Å with spectral resolution  $R \sim 2500 - 5000$  (Miller et al. 2024; Poppett et al. 2024).

The DESI MW Survey (MWS) is mainly performed at bright time (Cooper et al. 2023; Kposov et al. 2024), when the sky conditions are bright due to the moon phase, twilight, and worse seeing conditions making the observation of high redshift galaxies inefficient. The main MW survey will observe approximately 7 million stars selected from the DESI Legacy imaging Survey (Dey et al. 2019) to a limiting magnitude of  $r = 19$ . It covers most of the Northern Galactic cap region and a significant fraction of the Southern Cap region. DESI MWS also has a backup program (Dey, et al., in preparation), that is performed when the observing conditions are poorer with, e.g., very cloudy sky or too bright sky due to clouds, but with no threat of rain and the dome and telescope are usable for observations. It observes the spectra for several million stars mostly brighter than those observed in the main survey. The source selection of MWS backup program is based on *Gaia* photometry and astrometry, which does not rely on the photometry of the DESI Legacy imaging Survey, and it involves more stars at lower Galactic latitudes. In this study, we include stars from both the bright time and from the backup observations.

Following the Early Data Release (EDR; DESI Collaboration et al. 2024h) of DESI in June 2023, Kposov et al. (2024) published a DESI MWS stellar value-added catalogue for 400,000 stars, including commissioning and science validation data. The first data release (DR1) covering DESI Year-1 observation (observed from May 2021 through June 2022) will soon be made in the spring of 2025 (DESI Collaboration et al., 2025, in preparation). In this paper, we use the MWS data from DR1. Our stellar distance catalogue (SPECDis) is published as one of the Value Added catalogues (VAC) accompanying DESI DR1.

### 2.2 Data reduction and pipeline

DESI stellar spectra are processed first by the general Redrock spectral fitting code (Guy et al. 2023), followed by the pipelines specialized for stellar spectra (*rvs*, *sp* and *wd*). Our analysis in this paper depends on *rvs* and *sp*.

Here we provide a brief introduction to *rvs* and *sp*. Further details about all of the MWS pipelines is available in Cooper et al. (2023).

*rvs*<sup>2</sup> derives the radial velocities and atmospheric parameters using the algorithm of (Kposov et al. 2011). Interpolated stellar templates from the PHOENIX model (Husser et al. 2013) are fitted to the observed stellar spectra (without flux calibration).

By optimizing the log-likelihood combined across three arms simultaneously, it constrains the radial velocities, effective temperature ( $T_{\text{eff}}$ ), surface gravity ( $\log g$ ), iron abundance ( $[\text{Fe}/\text{H}]$ ), alpha-element abundance ratio ( $[\alpha/\text{Fe}]$ ), the projected stellar rotations and their corresponding uncertainties.

*sp* determines stellar atmospheric parameters by inferring individual elemental abundances. It is based on the FORTRAN code, FERRE<sup>3</sup> (Allende Prieto et al. 2006), with a new Python package written specifically for MWS, PIFERRE<sup>4</sup>. Only stellar spectra which have been successfully processed by *rvs* will be further passed to *sp*. *sp* stores the continuum normalized data spectra in the rest frame, the best-fitting model spectra with and without continuum normalizations.

In this paper, we are using the data product output by the *rvs* pipeline, which we call as *rvs* tables. The *rvs* tables also provide information about spectroscopic fiber information and the cross matched *Gaia* DR3 information. We use the continuum normalized spectra in rest frame produced by the *sp* pipeline.

### 2.3 Training and test stellar samples

Many previous studies apply relative error cuts to parallax for their training sample (e.g. Xiang et al. 2021; Wang et al. 2022). Moreover, S/N cuts to the stellar spectra are often adopted as well, to ensure high quality spectra utilized for training. However, such selections would limit the training sample to those stars with brighter apparent magnitudes and also at much nearer distances. This would cause the training sample to have parallaxes biased towards higher values compared with those more distant stars, and hence may result in significantly biased prediction in their absolute magnitudes and distances.

To avoid such selection effects, in this paper we choose not to apply any cuts in parallax error or the S/N of our stellar spectra. This would, however, result in a training sample with significantly less precise parallax measurements and lower quality stellar spectra. To overcome the lowered precision in parallax, we instead include the error in parallax measurements in the loss function adopted to optimize the network, to allow the training process to distinguish high and low precision parallax measurements (see Section 3.2.1 for details about the loss function), while not biasing the property distribution of our training sample. In this paper, the training sample and the full sample awaiting distance predictions based on the training outcome are identical. *Gaia* parallax is adopted for training, but our measured distances are much more precise than those inferred from *Gaia* parallaxes beyond 7 kpc, mainly due to the additional information brought in by the DESI stellar spectra and the inclusion of parallax uncertainty in the loss function, and we will back discussing this point later in Section 4.2. We also adopt PCA to reduce the noise and the dimensionality in the input stellar spectra (see Section 3.1 for more details), which would help to significantly decrease the scatter in our distance measurements for faint stars with low S/N stellar spectra.

In this paper we use *Gaia* DR3 parallaxes for our training, but

<sup>2</sup> <https://github.com/segasai/rvspectfit>

<sup>3</sup> <https://github.com/callendeprieto/ferre>

<sup>4</sup> <https://github.com/callendeprieto/piferre>

there are other distance measurements (e.g. [Das & Sanders 2019](#); [Bailer-Jones 2023](#)). In particular, most stars in our sample also have the [Bailer-Jones \(2023\)](#) distance measurements. However, we find that the [Bailer-Jones \(2023\)](#) distances show some under estimates for distant halo stars, as validated using member stars of known dwarf galaxies (see Appendix C). *Gaia* DR3 parallaxes, on the other hand, are approximately unbiased up to 100 kpc, despite of the large scatters at larger distances. Thus in this paper we choose to adopt the *Gaia* DR3 parallaxes for training and focus on the distances and geometric magnitudes inferred from *Gaia* DR3 parallaxes.

The selections we apply to our sample of stars are  $[\text{Fe}/\text{H}] > -3.9$  and  $E(B-V) < 0.5$ , to avoid extremely metal-poor stars and stars with significant extinctions. Moreover, we only use stars with  $\text{RVS\_WARN}=0$  (from the RVS table), which ensures that the stars can have robust stellar model fits by the rvs pipeline<sup>5</sup>. It is a bit mask flag which indicates potential issues or warnings related to the radial velocities measurements and stellar parameter determinations. The first bit of  $\text{RVS\_WARN}$  will be set to 1 if the discrepancy in the  $\chi^2$  values between the best-fit stellar model and the continuum model is small. The second bit is set to 1 if the radial velocity is  $\pm 5$  km/s close to the predefined velocity boundary ( $-1500$  to  $1500$  km/s). The third bit is set to 1, if the radial velocity uncertainty surpasses 100 km/s. A spectrum that does not exhibit any of these concerns is indicated by a  $\text{RVS\_WARN}$  value of zero. In addition, we retain only stars with *Gaia* RUWE<sup>6</sup> values smaller than 1.2 and *Gaia* PHOT\_VARIABLE\_FLAG != VARIABLE, which can help to eliminate some possible binary stars (see more details in Section 5 below) and remove photometrically variable stars. After these selections, we end up with 4 million unique stars without duplicates. We then divide these stars into the training and test samples. The training sample contains a 80% random subset of the total sample, which includes  $\sim 3.2$  million stars, and the remaining 20% test sample contains  $\sim 0.8$  million stars.

Because sources in the DESI backup observation are selected from *Gaia* instead of the photometry of the DESI Legacy imaging Survey ([Dey et al. 2019](#)), and we have included backup sources in this paper, we will utilize *Gaia* *G*-band flux throughout this paper, with extinction corrections. As the DESI footprint is at high Galactic latitudes, the 2-dimensional dust map is good enough for dust correction. In this work, we utilize the [Schlafly & Finkbeiner \(2011\)](#) dust map. We get the extinction coefficient for *Gaia* *G* from [Sartoretti et al. \(2023\)](#). The astrometric parallax measurements are taken from *Gaia* DR3, with zero-point corrections applied following [Lindgren et al. \(2021\)](#).

## 2.4 Stellar spectra

We start from the continuum normalized stellar spectra in rest frame processed by the DESI MWS *sp* pipeline. DESI bad pixel masks have been used to exclude such pixels in the stellar spectra. Here the bad pixel mask varies for each individual star, but our PCA (see Section 3.1 below) requires the same dimension of data. However, if a bad pixel mask happens for only a given star, while we mask this pixel for all stars, this would greatly reduce the number of pixels and result in a significant loss of information. Therefore, for a given pixel

that is a bad pixel for more than 10 % of the stars in our sample, we remove this pixel for all stars, and in this way we remove about 50 pixels. For the other bad pixels, we simply set the pixel value to zero, and we keep it zero throughout the entire spectral processing procedure below. For these pixels that have been set to zero in this way, most of the other stars have good reads, and thus PCA can still extract principal information from these pixels (see: Section 3.1) without being affected by a small amount of stars having zero pixel values.

The DESI *Z*-arm spectra cover the rest-frame wavelength range of 7,400-9,873 Å, which is severely contaminated by sky lines, and thus we discard the *Z*-arm spectral data entirely. Moreover, the DESI *R*-arm is also contaminated by sky lines, prompting us to create specific windows to mask these regions. Figure 1 shows the typical error spectra in log by stacking the errors of 50,000 randomly selected stars. We can notice several prominent sky lines, corresponding to large errors. The red brackets in Figure 1 mark the windows that are masked due to the existence of sky lines. Note the red end of *B*-arm and the blue end of *R*-arm can have a narrow overlapping region, i.e., duplicated wavelength. We connect *B* and *R*-arm data by taking the pixel reads from either arms to the middle point of this overlapping region. In the end, we end up with 5,500 pixels for each spectrum.

Ultimately, to more efficiently extract information from the stellar spectra, we perform some simple yet crucial transformations of the spectra. First, we believe that the absorption lines contain the most useful information. Therefore, we subtract the mean from the continuum normalized spectra, which have already been masked for bad pixels and sky lines. This is to increase the importance of pixels associated with absorption lines. Then we apply the following logarithmic transformation to the stellar spectra to reduce the impact of very large pixel values<sup>7</sup> in the spectra due to noise.

$$S_k = \begin{cases} \log(L_k + 1) & \text{if } L_k > 0, \\ -\log(-L_k + 1) & \text{if } L_k \leq 0, \end{cases} \quad (1)$$

here  $L_k$  is the value of the  $k$ -th pixel after the mean is subtracted from the continuum normalized spectrum in rest frame, and  $S_k$  is the value of the  $k$ -th pixel after logarithmic transformation. Note because we have subtracted the mean from the spectra,  $L_k$  can be negative. We take the negative sign of  $L_k$  when it is smaller than zero, and we add unity to make sure that the quantity is positive before logarithmic transformation. We have verified that the above transformation can lead to better precisions in our results, as taking the log operations can help us eliminating some extreme pixel values due to noise. For example, the blue end of *B*-arm data is usually very noisy, which can have large pixel reads that are about or more than 100-1000, hence dominating the loss function. Without taking log, these values can sometimes easily affect the precision in the training outcome. Sometimes even prevent the training from properly converging. Lastly, we recognize that the normalization of each stellar spectrum is not a constant, and we choose to normalize each stellar spectrum,  $S(\lambda) = \{S_k\}$ , by  $\sqrt{\sum_k S_k^2}$  before doing PCA (see Section 3.1 below).

## 2.5 External validation samples

The training and test samples are simply randomly divided subsamples from the parent sample. Although they do not overlap with each

<sup>5</sup>  $\text{RVS\_WARN}$  is a quality control flag output by

<sup>6</sup> RUWE stands for Renormalised Unit Weight Error. For stars with a significantly greater than 1.0 value of RUWE, it maybe a non-single star or has problematic astrometric solution. Detailed definition about RUWE can be found in [http://www.rssd.esa.int/doc\\_fetch.php?id=3757412](http://www.rssd.esa.int/doc_fetch.php?id=3757412).

<sup>7</sup> Some large pixel values can directly affect the training outcome, leading to results that do not easily converge.

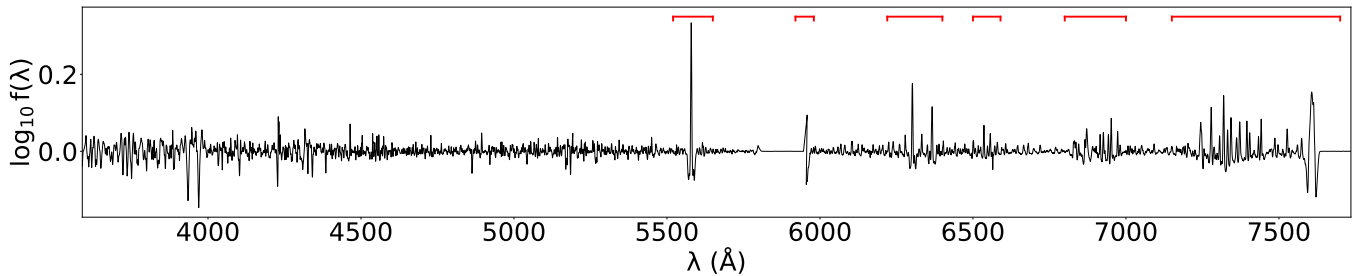


**Figure 1.** An example of coadded error spectra in log (y-axis), obtained by stacking 50,000 individual error spectra. Here  $f(\lambda)$  denotes the flux of error spectra after moving average. The regions of sky lines, marked by red brackets, are discarded. The range devoid of skylines are utilized for PCA.

other, and the test sample provides some validations on the training outcome, we still require some independent external validations to verify our distance measurements out to large distances, where the *Gaia* parallaxes have very large uncertainties.

In this paper, we utilize member stars from GCs, dwarf galaxies, the Sagittarius stellar stream (Sgr) and blue horizontal branch (BHB) stars from DESI Year-1 data with accurately known distances, as our external validation sample. We cross match our sample of stars (Section 2.3) with the member star catalogues of GCs and dwarf galaxies by Baumgardt & Vasiliev (2021) and Pace et al. (2022). Most of these matched stars are observed in the backup program. The typical relative distance uncertainty for GCs is smaller than 1%, and for dwarf galaxies it is  $\sim 5\%$ , ensuring their member stars can have accurate distance estimates. These member stars are selected based on their spatial distributions, *Gaia* proper motions and parallaxes, to build up probabilistic mixture models to distinguish true members and fore/background stars. The member stars from Sgr are from Vasiliev et al. (2021), with their distances calibrated using RR-Lyrae stars, with typical relative distance errors of  $\sim 10\%$ . Details about the BHB sample in DESI can be found in Byström et al. (2024). There are in total 6,327 BHB stars in Year-1 data. After removing duplicates and member stars belonged to GCs, dwarf galaxies and Sgr, there are 4565 stars.

We cross match these GCs, dwarf galaxies and stream member stars and our stellar sample according to their coordinates, and adopt the distances from these studies as our reference distances. For BHB stars, we cross match with our stellar sample by DESI TARGETID, i.e., DESI source ID. Details about the BHB distance measurements can be found in Byström et al. (2024). In this paper, we will denote the accurate distance modulus inferred from these member stars by  $(m - M)_{\text{true}}$ .

For the matched stars, we further utilize their radial velocities (RVs) in DESI to select secure member stars. We first calculate the average and  $1-\sigma$  scatter in their RVs. We maintain only those stars whose RVs differ by less than  $2-\sigma$  from the average RVs for validations. Ultimately, we have 2,154 member stars from GCs (mainly covering 5 to 20 kpc), 320 member stars from dwarf galaxies (covering 80-100 kpc, and several stars could approach 200 kpc), 1,001 member stars from Sgr (25-60 kpc) and 4,326 stars from DESI Year-1 BHB sample (8-100 kpc). Nearby GC member stars can include both main sequence stars and giants, while member stars from Sgr and more distant dwarf galaxies are all giants.

### 3 METHODOLOGY

In this section we introduce the application of PCA to the DESI stellar spectra, the neural network methodology and the error model for the SpecDis VAC.

#### 3.1 PCA to reduce the noise and dimensionality in the data spectrum

The observed stellar spectra contain noise. Although we have performed a logarithmic transformation on the original spectra to mitigate the impact of some very large pixel values caused by noise (see Section 2.4 above), noise still exists in the spectra to affect the precision in distance prediction. Furthermore, our entire sample of stellar spectra is a huge data cube. After cutting out bad pixels and sky lines, 5,500 pixels are left in each spectrum, and we have a total of about 4 million spectra. However, most of the pixels do not contain useful information, except for those pixels belonging to absorption lines.

To reduce the noise in the input spectra, and also to reduce the dimensionality of the input data set, we adopt PCA. This follows the idea of Xiang et al. (2021). PCA is a standard multivariate analysis technique that is frequently utilized in many different fields of astronomy and astrophysics (e.g. Budavári et al. 2009; Chen et al. 2012; Zhou et al. 2023b). The concept of PCA applied to data spectra is that a spectrum with  $N$  pixels can be regarded as a single point in an  $N$ -dimensional space. A group of spectra therefore form a cloud of points in this high-dimensional space. PCA searches for  $N$  vectors, known as principal components (PCs), which have decreasing orders of variance in the cloud of points. Each time a PC with the highest variance is determined, the succeeding PC in turn to be searched should have the highest variance under the constraint that it is orthogonal to or uncorrelated with the preceding components.

After deducing the  $N$  vectors or PCs, the  $i$ -th stellar spectrum, which we define and denote as  $S(\lambda)_i = \{S_{i,k}\}$  can be decomposed as,

$$S_{i,k} = \sum_j C_{i,j} E_{j,k} + R_{i,k}, \quad (2)$$

where the index  $k$  represents the  $k$ -th pixel.  $E_{j,k}$  represents the  $k$ -th pixel value for the  $j$ -th PC, and  $C_{i,j}$  is the corresponding coefficient for  $j$ -th PC.  $\sum_j C_{i,j} E_{j,k}$  gives the reconstructed spectrum for the  $i$ -th stellar spectrum, and we denote the reconstructed spectrum by  $S(\lambda)_{i,\text{reconstruct}} = \{S_{i,k,\text{reconstruct}}\}$ .  $R(\lambda)_i = \{R_{i,k}\}$  is the associated residual.

We show in Appendix A (Figure A1) the first ten PCs. It is clear

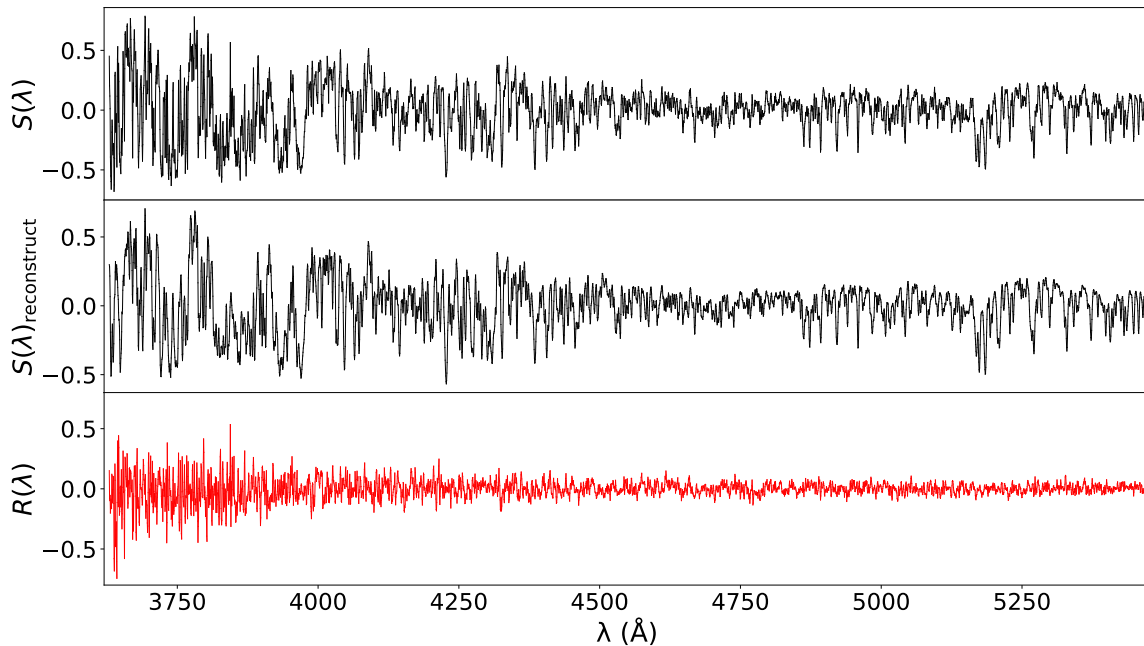


**Figure 2.** An example of PCA reconstruction, focusing on a DESI B-arm spectrum with a S/N of 3 for a randomly selected star. Here  $S(\lambda)$  in the top panel denotes the log flux of stellar spectra after subtracting the mean and after logarithmic transformation (Equation 1 and Section 2.4). The middle panel shows the reconstructed spectrum based on the first 100 principal components. The bottom panel shows the residuals.

that these PCs successfully capture the line information in the stellar spectra, and also contain features of cool stars. Figure 2 shows an example of reconstruction using the first 100 PCs, that is, the summation of Equation 2 is only for the first 100 PCs. Higher order PCs are not used. The S/N of the original spectrum is only 3. The reconstructed spectrum using the first 100 PCs is shown in the middle panel, which is less noisy. The bottom panel shows the residual, which is dominated by noise. It is straight-forward to understand the reduction of noise by using the reconstructed spectra from several top important PCs, if their largest variances correspond to the most useful information in the original stellar spectrum. On the other hand, we expect the remaining less important PCs to become more and more dominated by noise.

Figure 2 clearly demonstrates the reduction of noise with the reconstructed spectrum from the first 100 PCs. In fact, we have experimented with different numbers of top PCs, ranging from several tens to 1,000, and we have found that there is no improvement beyond the choice of 100. Moreover, based on the key concept of PCA, using the 100 coefficients,  $C_{i,1-100}$ , is equivalent to using the reconstructed spectrum from the first 100 PCs, and thus we will utilize the first 100 coefficients for each star for neural network training, instead of the spectrum, throughout this paper. This approach naturally helps us to reduce the dimensionality in the data cube as well.

Figure A2 in Appendix A presents the correlations between the [Fe/H] abundance, effective temperature and the coefficients of the top two PCs and the 100-th PC. It is clear that the coefficients of the top PCs are correlated with these physical features, and the coefficient of the hundredth PC shows less correlation. We also confirmed that higher-order PCs show almost no correlations with the stellar features.

## 3.2 The Neural Network Models

### 3.2.1 Training Label and Loss Function

Neural network (NN) establishes the connection between the input stellar spectra and the quantity to be predicted, and the predicted quantity is called label. To establish this connection, usually an appropriate loss function is defined at first, that is going to be minimized to achieve the best trained model and properly establish the connection. In this section, we introduce our choice of the label and the loss function.

In this paper we do not choose the absolute magnitude as our label as in some previous works (e.g. Xiang et al. 2021; Wang et al. 2022). Instead, we utilize the reciprocal of the square root of luminosity (Equation 3) as our label, i.e., the NN will predict the label defined by Equation 3 below for each star

$$\text{label} \equiv \frac{1}{\sqrt{L_G}} \equiv \frac{\omega}{10^{2-m_G/5}} \equiv \frac{\omega}{\sqrt{F_G}}. \quad (3)$$

Here  $\omega$  is the *Gaia* parallax.  $L_G$  is the *G*-band luminosity. The deduction is based on the relation between absolute magnitude ( $M_G$ ) and apparent magnitude ( $m_G$ ) of  $m_G - M_G = -5 \log_{10} \frac{\omega}{100}$ , where  $\omega$  is in units of mas, and  $M_G = -2.5 \log_{10} L_G$ .  $F_G$  is the observed flux in *Gaia G* band, and is related to the apparent magnitude as  $\sqrt{F_G} = 10^{2-m_G/5}$ .

There are several advantages of using this label over directly using the absolute magnitude or luminosity. First of all, with this label, there is no need to remove stars with negative *Gaia* parallax from the sample, but if we take the absolute magnitude as the label, negative parallax values have to be removed, leading to bias in the training sample. In fact, our neural network predicts that a non-negligible

fraction of these stars with negative parallaxes are located beyond 15 kpc from the Sun, and we find that if stars with negative parallaxes excluded from our training sample, there will be biases in the predicted distances for more distant stars.

Moreover, the error in the observed flux is expected to be very small, so the error on parallax dominates Equation 3. Since Equation 3 is linear in parallax, we can expect the overall prediction remains unbiased, even if including objects with very large parallax uncertainties.

In machine learning, the loss function is a function that measures the difference between the predicted label and the true label in a NN model. It quantifies the performance of a machine learning model by evaluating how well model prediction matches the true data. Once the NN predicts the label for the  $i$ -th star,  $\text{label}_i$ , the loss function is constructed with respect to parallax, as shown by Equation 3 below:

$$\chi^2 = \sum \frac{(\text{label}_i \times 10^{2-m_{G,i}/5} - \omega_i)^2}{\sigma_{\omega_i}^2}. \quad (4)$$

Basically, our loss function is a  $\chi^2$  statistic.  $\omega_i$  and  $\sigma_{\omega_i}$  are the *Gaia* parallax and parallax error for star  $i$ , and  $m_{G,i}$  is the apparent magnitude. The summation is over all stars in the training sample. Although we choose not to include any cuts on parallax error for our training sample, the loss function in Equation 4 above naturally assigns smaller weights to stars with larger parallax errors in the training process. Most importantly, although stars with large parallax errors contribute less due to their smaller weights, they are not completely discarded. This ensures that our training sample is not biased towards only very nearby stars.

Ultimately, we obtain the distance or distance modulus by using the predicted label, which provides the luminosity or absolute magnitude, and compare it with the observed apparent magnitude of each star.

### 3.2.2 Neural Network Structure

We adopt a feed-forward multilayer perceptron NN model that maps the first 100 coefficients of PCs to the label defined in Equation 3 above. Here feed-forward means all information flows forward only in the network. Multilayer refers to the structure of a NN that is composed of multiple layers, where each layer is connected to the next layer. Adopting the Einstein summation convention, our NN contains four layers and can be written as

$$\text{label} = w_k^3 I(w_{jk}^2 (w_{ij}^1 I(w_{\lambda i}^0 f_{\lambda} + b_i^0) + b_j^1) + b_k^2) + b^3, \quad (5)$$

where  $I$  is the ReLU<sup>8</sup> activation function,  $w$  and  $b$  are weights and biases of the network to be optimized, which we call neurons, and  $f$  denotes the coefficients of PCs. We adopt 100 neurons for all four layers. The so-called perceptron represents a single neuron-like unit that performs a specific computation.

## 3.3 Error Model

In this section, we discuss the methodology for quantifying the measurement uncertainty. For simplicity, we will transform the NN-predicted label of  $1/\sqrt{L_G}$  (see: Section 3.2.1) to the absolute mag-

nitude ( $M_{G,NN}$ ) for the remainder of this paper. We will present the estimated error statistics in Section 4.3.2.

### 3.3.1 Measurement Uncertainty for each star

NN does not directly output error estimates, however we provide error estimates for  $M_{G,NN}$  and our final measured distances. These estimates are obtained through Monte-Carlo sampling the error spectra of individual stars. Here the error spectra gives the associated error for each pixel read of the stellar spectra, which encompass a combination of read-out noise, Poisson errors and errors in sky subtraction by the pipeline. We start with the continuum normalized stellar spectra in the rest frame, to which we add Gaussian noise in accordance with the error spectrum read at each pixel.

This process is repeated to generate twenty randomly perturbed versions of each spectrum. We then repeat all steps outlined in 2.4 to process each perturbed spectrum: subtracting the mean, taking the logarithm, and normalizing the spectrum. Subsequently, PCA is utilized to reduce the noise and dimensionality. Notably, the PCs are fixed to be those we obtained in Section 3.1 based on the data spectra. We did not do PCA again for each set of perturbed spectra, but instead we utilize the same set of PCs for decomposition and getting the coefficients. Finally, we input the coefficients of the top 100 PCs into our trained NN to obtain twenty sets of  $M_{G,NN}$  or distance for each star.

The standard deviation of these values serves as the measurement uncertainty of  $M_{G,NN}$  or distance for each star. In our analysis, we have chosen to ignore the uncertainties from the apparent magnitudes of each star, as the photometric uncertainties are much smaller than those from the noisy stellar spectra.

### 3.3.2 Training uncertainty

The inherent uncertainty of NN is estimated by training several individual NNs. Each NN is initialized with a distinct random seed to start the training, thereby yielding some different estimates of  $M_{G,NN}$  and distance for each star in our sample. However, we do not estimate the uncertainty of each individual star as in Section 3.3.1 above, because the uncertainty is an intrinsic feature of NN model, so it is expected to be a fixed value instead of varying among different stars. The uncertainty is the standard deviation of the difference between different NN predicted  $M_{G,NN}$ . We find that this uncertainty is typically about 0.05 magnitude. The total uncertainty of a star is the square root of sum of the measurement and training uncertainties added in quadrature.

## 4 RESULTS

In this section, we will test and validate the accuracy of our SPECDis VAC, using both the test sample and an independent external validation sample. Ultimately, we will present statistical summaries of our distance catalogue for the DESI Year-1 data.

### 4.1 Validation on the test sample

Figure 3 compares the NN predicted absolute magnitude,  $M_{G,NN}$ , and the absolute magnitude calculated from *Gaia* parallax with zero point corrections (Lindegren et al. 2021),  $M_{G,geo}$ . To have a robust validation, Figure 3 is based on a subset of the test sample with precise *Gaia* parallaxes, that we require the relative parallax error to be smaller than 10%, i.e.,  $\sigma_{\omega}/\omega < 0.1$ , so that we can use the

<sup>8</sup> ReLU is an activation function, which returns 0 when the inputs are smaller than 0 and returns the original values if the inputs are greater than or equal to 0.

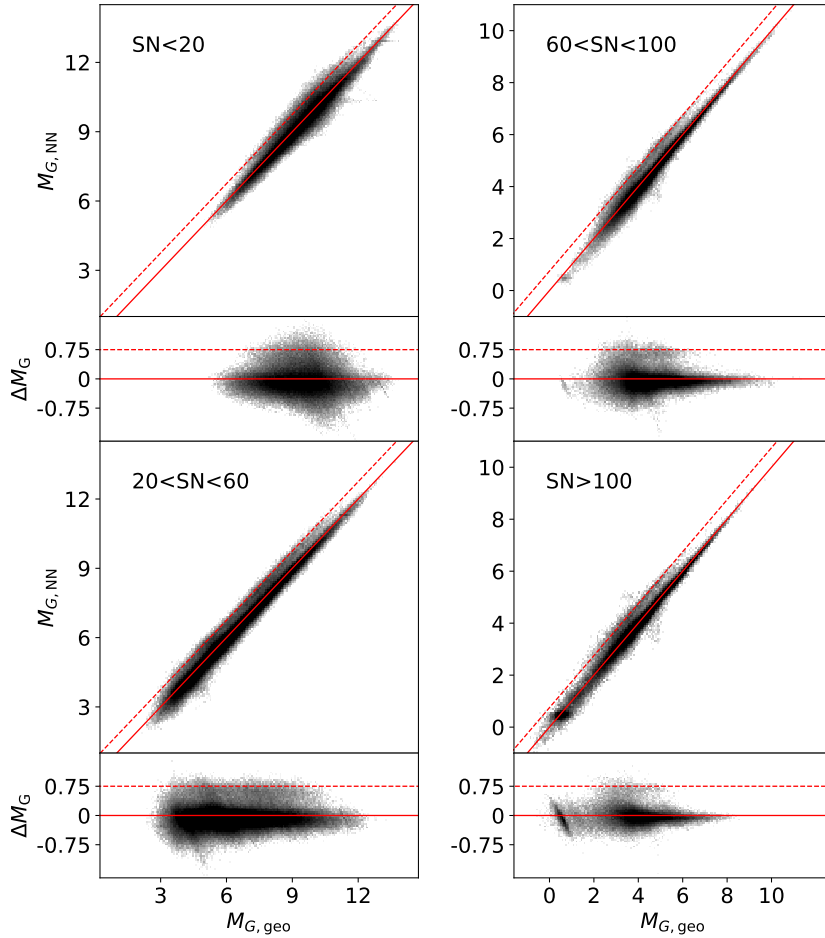


**Figure 3.** Comparison between  $M_{G,\text{NN}}$  and  $M_{G,\text{geo}}$ . This is based on stars with precise *Gaia* parallax measurements ( $\omega/\sigma_\omega > 10$ ) of the test sample to deduce the geometric magnitude,  $M_{G,\text{geo}}$ , so that  $M_{G,\text{geo}}$  can be used as the reference to be compared with our measured  $M_{G,\text{NN}}$ . Four subsamples are shown according to different ranges in S/N of their spectra, with the S/N range shown by the text in corresponding panels. The residuals of  $\Delta M_G = M_{G,\text{NN}} - M_{G,\text{geo}}$  are also shown at four lower bottom panels. The red solid line marks  $M_{G,\text{NN}} = M_{G,\text{geo}}$ , and the dashed line offset by 0.75 magnitude from the red solid line. There are two-band structures: single stars are distributed along the solid line, while the dashed line may correspond to binary systems (further detailed in Section 5).

precise parallax measurements to deduce precise  $M_{G,\text{geo}}$  as the reference for comparison. We show results based on four subsamples with different S/N ranges<sup>9</sup>, as indicated by the text in corresponding panels. We show both  $M_{G,\text{NN}}$  versus  $M_{G,\text{geo}}$  and the difference between  $M_{G,\text{NN}}$  and  $M_{G,\text{geo}}$  ( $\Delta M_G$ , i.e., the residual) as a function of  $M_{G,\text{geo}}$  in corresponding lower panels for each subsample. All panels demonstrate high precision for  $M_{G,\text{NN}}$  with no particular bias, even in the panel with the lowest S/N. As S/N increases, the scatter of  $M_{G,\text{NN}}$  decreases. The 1- $\sigma$  scatter from the lowest to the highest S/N panels are 0.48, 0.26, 0.24 and 0.22 magnitudes, which correspond to distance uncertainties of 24%, 13%, 12%, and 11%, respectively. Here we have adopted PCA (see Section 3.1) to reduce

the noise in the spectra and have been using the coefficients of the top 100 PCs for the training and prediction, so the scatter is significantly reduced. If using the original noisy data spectra, the scatter can be significantly larger. For example, the scatter can be as large as 0.9 magnitudes for S/N > 20.

Figure 3 shows a two-band structure, which is expected when binaries are present. The sources that fall along the red solid diagonal line are single stars, and the red dashed line represents the binaries. For these latter sources, the predicted  $M_{G,\text{NN}}$  is fainter than the geometric magnitude  $M_{G,\text{geo}}$ , because  $M_{G,\text{geo}}$  is the combined magnitude from two stars, so this shifts binary stars away from the diagonal line. In all panels, the red dashed line, which presents the binary band, is shifted upwards by 0.75 magnitudes from the red solid line. This corresponds to equal-mass binaries. For equal-mass binary system, the

<sup>9</sup> The S/N is defined as the average S/N of the *B* and *R* arms.

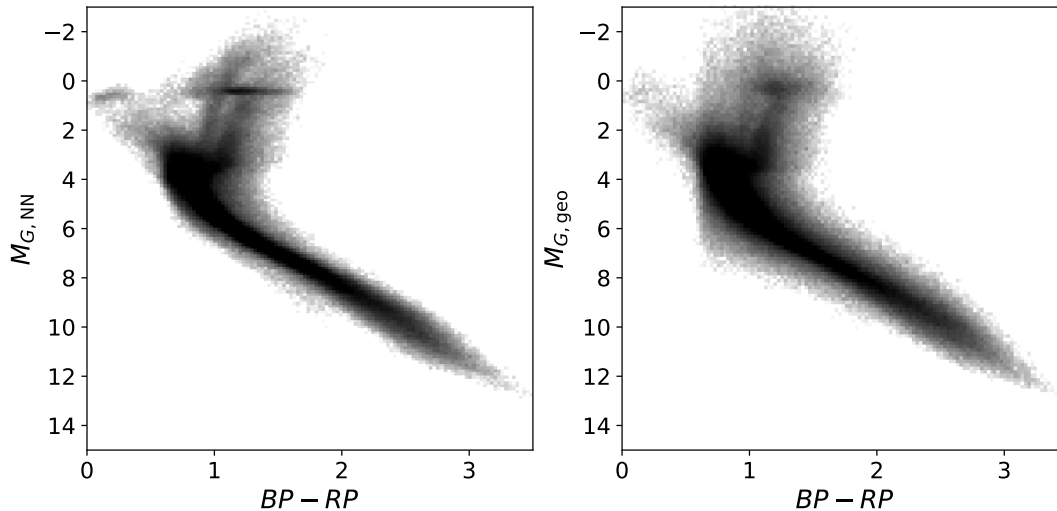


**Figure 4.** The Hertzsprung-Russell diagram based on the full test sample. The x-axis of two panels are the colour index derived from the mean magnitudes of the *Gaia* photometry in the *BP* and *RP* bands. The y-axis of the left panel represents the NN predicted absolute magnitude,  $M_{G, \text{NN}}$ . The y-axis of the right panel shows the absolute magnitude deduced from *Gaia* parallax,  $M_{G, \text{geo}}$ , without any cuts on parallax error. Negative parallaxes are excluded from the right plot.

combined flux doubled, so the geometric magnitude of the two stars is expected to be 0.75 magnitudes brighter than that of a single star, while the NN predicted  $M_{G, \text{NN}}$  from the stellar spectrum remains equivalent to that of a single star because two equal-mass stars have similar spectral types, and thus the combined spectrum remains the same as that for a single star.

With the decrease in S/N, however, the binary band becomes less distinct. Moreover, there appears to be a trend where the binary band shifts away from the single star band by less than 0.75 magnitudes as the S/N decreases. This is evident in the top left and bottom left panels, where most of the black dots fall below the red dashed lines. Perhaps this is because different S/N ranges correspond to stars in different regions of the Hertzsprung-Russell (HR) diagram, and the mass ratios of binaries can vary across the HR diagram.

Figure 4 shows the distribution based on the full test sample in the HR diagram. The x-axis represents the colour index derived from the mean magnitudes of the *Gaia* photometry in the BP and RP bands. And the y-axis of the two panels represent the NN-predicted *Gaia* G-band absolute magnitude (left panel) and the Geometric *Gaia* G-band absolute magnitude (right panel) deduced from *Gaia* parallax, without any selections on parallax errors. The left plot of figure 4 provides a sharper visual representation of the various evolutionary stages of stars within the test set than the right panel. Moreover, the relatively tight distribution of stars on the left panel, with reasonably small scatter compared to the right panel, demonstrates the reliability in our NN-predicted  $M_{G, \text{NN}}$ . As a comparison, the right plot, which is based on *Gaia* parallax without any error cuts, is significantly more fuzzy. The comparison shows that our distance measurements are more precise than those inferred from *Gaia* parallax. While we adopt *Gaia* parallax for training, the improvement seen here is mainly due to the additional information brought by the stellar spectra and the inclusion of parallax errors into the loss function. We will discuss this topic in greater detail in the next subsection.

Figure 5 displays whether the difference between  $M_{G, \text{NN}}$  and  $M_{G, \text{geo}}$  ( $\Delta M_G$ ) shows any dependence on stellar parameters,  $[\text{Fe}/\text{H}]$ ,  $[\alpha/\text{Fe}]$ ,  $T_{\text{eff}}$  and  $\log g$ , using the test sample. Here the stellar parameters are taken from the *rvs* table. While the scatter in  $\Delta M_G$  obviously

shows dependencies on stellar parameters, there is no obvious bias away from zero over the full range of stellar parameters probed here.

## 4.2 External Validation

In this section, we will validate our distance estimation by comparing the NN predicted distance modulus with those from the external validation set, which has accurate distance measurements that can be used as the reference (see Section 2.5 for details). With such a validation set, we aim to rigorously assess the accuracy and reliability of our NN predicted distances.

Figure 6 shows the comparison between NN predicted distance modulus  $(m - M)_{\text{predict}}$  and reference distance modulus  $(m - M)_{\text{true}}$ , which we take from the external catalogue of GC, dwarf and stream member stars, with the uncertainty of  $(m - M)_{\text{true}}$  being negligible.

The left panel of Figure 6 covers a distance modulus range from 14 to 22 magnitudes, corresponding to a distance range from approximately 6 kpc to 250 kpc. The  $1-\sigma$  scatter of  $(m - M)_{\text{predict}}$  is about 1 magnitude, which corresponds to a distance uncertainty of about 50%. The  $(m - M)_{\text{true}}$  of most stars from GCs are smaller than 16 magnitude, and Sgr member stars span from 16 to 19 magnitude. Almost all member stars from dwarf galaxies have  $(m - M)_{\text{true}}$  greater than 19 magnitudes. The distribution of  $(m - M)_{\text{predict}}$  in the left panel is roughly centred around the diagonal line, indicating that our NN model exhibits no significant bias in its distance predictions.

The right panel of Figure 6 shows  $(m - M)_{\text{predict}}$  versus  $(m - M)_{\text{true}}$  after excluding stars with distance modulus errors<sup>10</sup> greater than 0.5 magnitudes. After excluding these stars, the prediction of  $(m - M)_{\text{true}}$  shows no bias when compared to the distribution observed in the left panel, and the scatter is significantly reduced.

The right panel of Figure 6 also demonstrates that the error model constructed in Section 3.3 is reliable. As the distance modulus uncertainty calculated from the difference between  $(m - M)_{\text{predict}}$  and

<sup>10</sup> The distance modulus error is equivalent to the error of  $M_{G, \text{NN}}$ , which is estimated by the method in Section 3.3.

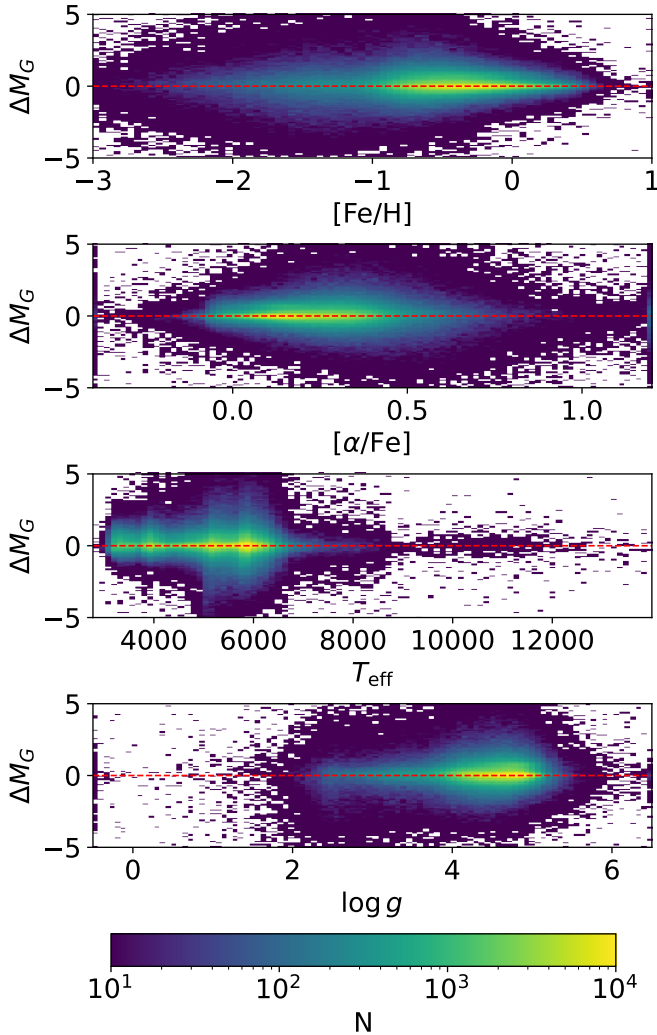


**Figure 5.** Difference between the NN predicted  $M_{G,\text{NN}}$  and  $M_{G,\text{geo}}$ , presented as a function of stellar parameters of the full test sample. The red dashed line shows  $\Delta M_G = 0$ .

$(m - M)_{\text{true}}$  of the right panel is roughly equal to the uncertainty threshold of 0.5 magnitude that we apply, which corresponds to distance uncertainty of 25%. It demonstrates that the uncertainty of  $(m - M)_{\text{predict}}$  estimated by NN is reliable. We will provide more details about the measurement error in Section 4.3.2 below.

However, for the most nearby and most distant stars in the left panel Figure 6, the prediction presents some bias. The distances are overestimated when  $(m - M)_{\text{true}}$  is around 14.5 magnitude, with  $(m - M)_{\text{predict}}$  being brighter than  $(m - M)_{\text{true}}$ . For a detailed overview of these predictions, see Table A1 in Appendix B, which lists the median values of the NN predicted distances for GCs and dwarf galaxies. Additionally, we show in Figure A3 of Appendix B the distribution of NN predicted distance modulus and geometric distance modulus from *Gaia* parallax for each of the GC, dwarf galaxy and different distance bins of Sgr. Most of the stars that are overestimated around  $(m - M)_{\text{true}} = 14.5$  in Figure A3 are from NGC 5904 and NGC 6205. There is a clear bias in the distribution of  $(m - M)_{\text{predict}}$  for NGC 5904 and NGC 6205 with respect to  $(m - M)_{\text{true}}$  (the red dashed vertical line), but the scatter is only about 0.25 magnitudes. We are uncertain about the cause behind the bias, and we have checked

that differences among various literature measurements cannot fully account for this bias. But after excluding the stars with distance modulus errors greater than 0.5 magnitudes, which is equivalent to excluding low S/N stars, there is no particular bias in the right panel of Figure 6.

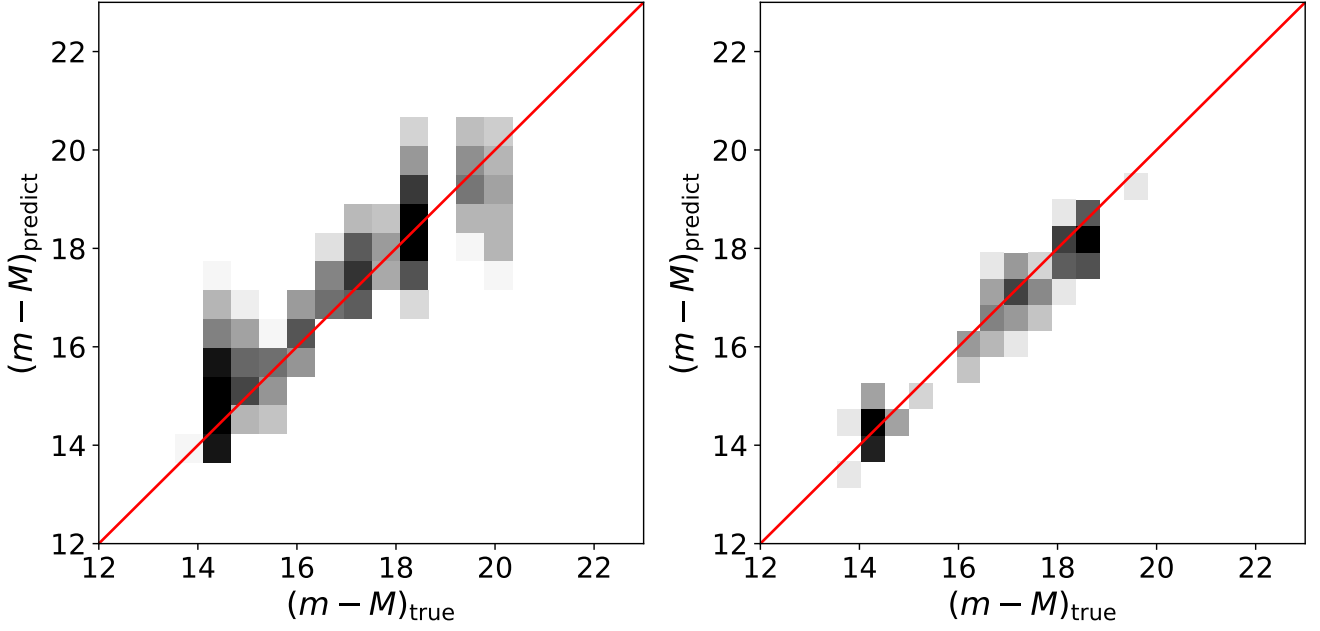
For the most distant stars ( $(m - M)_{\text{true}} > 19$ ) in the left panel of Figure 6,  $(m - M)_{\text{predict}}$  is underestimated compared to  $(m - M)_{\text{true}}$ . All of these stars are giants from dwarf galaxies. In fact, the number of stars with  $(m - M)_{\text{true}} > 19$  is quite few as shown in Figure A3 of Appendix B, and is mainly from Draco and Sextans. The slight underestimate in distance at  $(m - M)_{\text{true}} > 19$  may be attributed to the fact that the number of very distant stars is significantly less than the number of nearby stars, and distant stars also have lower weights in our loss function (see Equation 4). Notably, we did not apply any cuts on parallax error for our training sample (see Section 2.3), which has helped us to achieve much better estimates for distant stars. As we have tested, if adopting error cuts to select only stars with more precise parallax measurements, we will limit the training sample to stars that are much closer, and the distant stars in Figure 6 would suffer from significantly larger underestimates.

Despite the small amount of bias at the nearest and furthest ends, interestingly, Figure A3 of Appendix B clearly shows that our measured distances perform significantly better than those based on the *Gaia* parallaxes beyond 7 kpc. Our distances show much smaller bias and dispersion than the distances from *Gaia* parallaxes in NGC 6205 at 7.42 kpc and most of the other more distant systems, when the number of member stars is large enough. This proves the success in our methodology and the robustness of our distance measurements. Note again, our training and the sample awaiting distance predictions are identical. We utilize *Gaia* parallaxes for training, but the predicted distances are much more precise than *Gaia* parallaxes out to about 100 kpc as confirmed by this external validation.

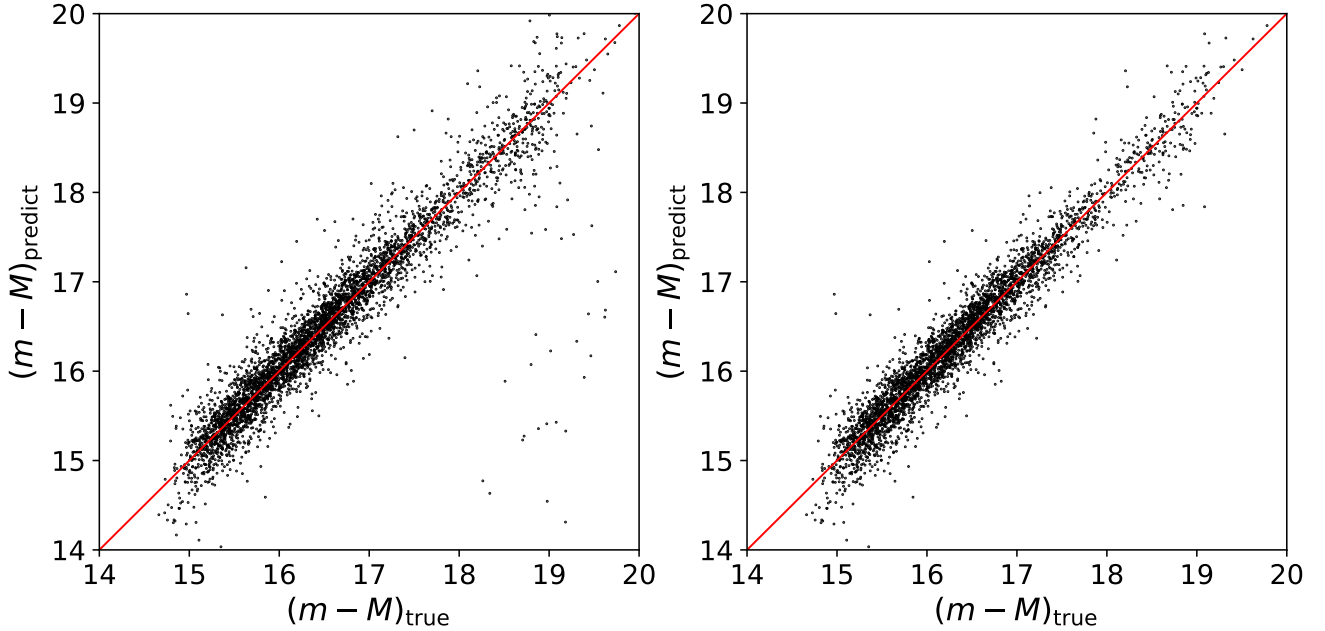
Our predicted distances are more precise than those inferred from *Gaia* parallaxes. This is mainly due to the additional information brought in by the DESI stellar spectra and the inclusion of parallax uncertainty in the loss function. For two stars with the same spectral type but different levels of parallax uncertainties, if the model can recognize that they have the same spectral type, the star with the more precise parallax measurement can provide additional information to recalibrate the luminosity and parallax of the other star. On the other hand, our loss function is a  $\chi^2$  variable written in parallax space, so sources with larger parallax uncertainties will be less dominant in the training process, while the training relies more on those stars with more precise parallaxes. However, for those stars with larger parallax uncertainties, though they are less dominant, they still contribute to the loss function. We do not completely discard them. This is important, because as previously mentioned, if we only adopt stars with precise *Gaia* parallax measurements for training, we bias our training sample to the nearby stellar population, which may not cover the more distant stellar population in the stellar parameter space. We also note that our training label (Equation 3) is linear in parallax, and thus the uncertainties of parallax can be cancelled out to some extent, in the end leaving on average an unbiased result (see Section 3.2.1 for details).

Figure 7 further presents the comparison between  $(m - M)_{\text{predict}}$  from our NN and  $(m - M)_{\text{true}}$  from DESI Year-1 BHB sample as reference. Similar to Figure 6, the left panel of Figure 7 does not include any distance error cut and covers a wide range of distance modulus from 8 to 20 magnitudes, which corresponds to a distance range from 8 to 100 kpc. The  $1-\sigma$  scatter is only 0.36 magnitude, corresponding to a distance uncertainty of 18%.

The right panel of Figure 7 excludes the BHB stars with distance



**Figure 6.** Comparison between NN predicted distance modulus,  $(m - M)_{\text{predict}}$ , and reference distance modulus,  $(m - M)_{\text{true}}$ . The reference distance modulus is from GCs, Sagittarius stream and dwarf galaxy member stars that can have a more precise distance measurement from their hosts or stream track. **Left:** All validation stars. **Right:** Stars with distance modulus error  $< 0.5$ , which correspond to a precision of 25% in distance.



**Figure 7.** Comparison between NN predicted distance modulus,  $(m - M)_{\text{predict}}$ , and reference distance modulus,  $(m - M)_{\text{true}}$ . The reference distance modulus is from DESI Year-1 BHB VAC. **Left:** All DESI Year-1 BHB stars. **Right:** Stars with distance modulus error  $< 0.5$ , which correspond to a precision of 25% in distance.

modulus errors greater than 0.5 magnitude, or about 12% of the BHB sample. After excluding these stars, the  $1\text{-}\sigma$  scatter of the remaining BHB stars is only 0.23 magnitudes, corresponding to a distance uncertainty of 12%.

The left and right panels of Figure 7 demonstrate that our distance measurement shows no bias for nearby and distant stars with smaller

scatter compared with Figure 6. We find that the median S/N of our BHB sample is 34, while the median S/N of member stars in our GCs, dwarf galaxies, and Sgr external validation sample are only 9, 11 and 13 respectively. Thus S/N dominates the precision of our prediction. Lower S/N leads to the larger scatter and slight bias in the left plot of Figure 6.

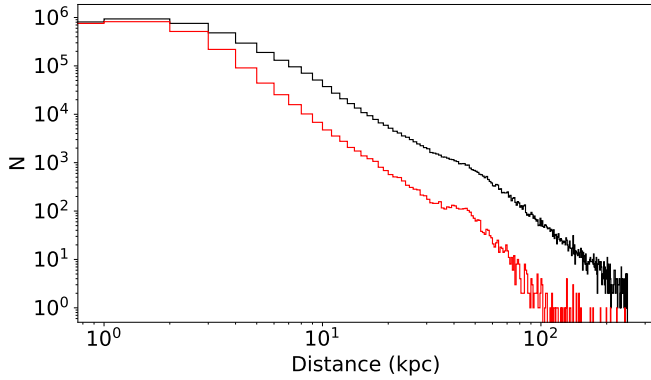


**Figure 8. Black line:** Distribution of heliocentric distance of the full sample. **Red line:** Distribution of heliocentric distances of stars with relative distance error smaller than 25%.

Figures 6, 7 and A3 of Appendix B demonstrate that our NN predicted distances are reliable after applying an appropriate distance error cut and demonstrate no significant bias up to  $\sim 100$  kpc. The distance catalogue used in this work is considered credible because of its thorough validation against independent distance measurements, rigorous error analysis, and transparency in the methodologies applied. These factors ensure a high level of confidence in the accuracy of the distances provided.

### 4.3 Statistics of the Distance catalogue

In this section we present some basic statistics of SPECDis. Note distances are derived from  $M_{G,NN}$ , and the associated uncertainties are estimated according to the method of Section 3.3.

#### 4.3.1 Distance

In total, SPECDis includes the absolute magnitudes and distances for about 4 million stars. Figure 8 presents the number of stars as a function of heliocentric distance in log space. The black histogram shows the radial distribution of all stars. Our measurements cover a wide range of distance. Most of the stars are located within 15 kpc from the Sun. About 120,000 stars have distances greater than 15 kpc (about 40% of them have negative parallaxes but we can predict positive distances for them), and about 20,000 have distances larger than 50 kpc from the Sun. A number of stars could even lie beyond 200 kpc. Note our choice of not applying any cuts on *Gaia* parallax error in the training sample has greatly helped to extend the measurements out to large distances. The red histogram shows those stars with relative distance error smaller than 25%. This results in a much smaller sample.

Both the red and black histograms in Figure 8 appear to show a double power-law form, with the break radius at about 50 kpc. The existence of break radii in the radial density profile of MW stellar halo has been reported in many previous studies (e.g. Watkins et al. 2009; Deason et al. 2011; Hernitschek et al. 2018; Han et al. 2022). The break radius can reflect the transition from a disk-dominated region to a halo-dominated region. Moreover, it may indicate a massive accretion event. However, Figure 8 here only shows a very preliminary radial distribution of stellar number counts, without correcting for any selection effects of the survey. We leave more detailed investigations of the density profile of the MW stellar halo to a future study.

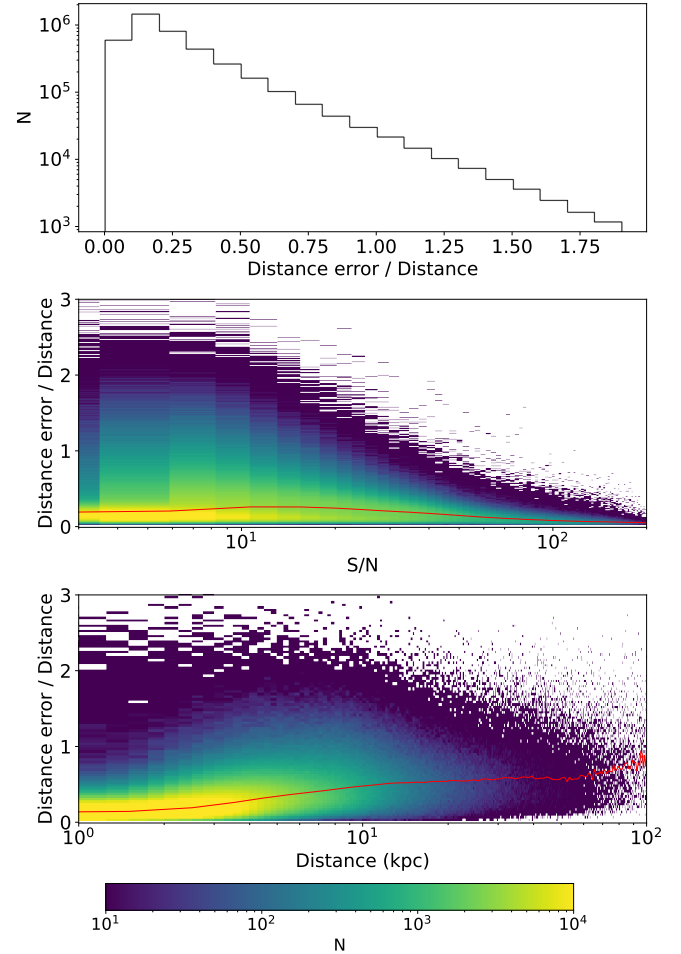


**Figure 9. Top:** Distribution of relative distance uncertainty of the total sample. **Middle:** relative distance uncertainty as a function of S/N. The red line shows the median value of the relative error at various distances. **Bottom:** Relative distance uncertainty of the total sample as a function of distance, the distance uncertainty is derived by the method of Section 3.3. The red line shows the mean value of the relative error at various distances.

#### 4.3.2 Distance Uncertainty

Figure 9 displays three plots: the distribution of relative distance uncertainty (top plot), relative distance uncertainty versus S/N of the total sample (middle plot) and the relation between relative distance uncertainty and distance (bottom plot). Here the uncertainties are all derived from the method<sup>11</sup> It is also different from the external validation in Section 4.2. in Section 3.3. We find that the relative distance uncertainties of most stars are smaller than 50%. About 60% of the stars have a relative distance uncertainty of less than 25%.

The middle panel of Figure 9 shows that the distance uncertainty is related to S/N. The relative distance uncertainty is decreasing with increasing S/N when S/N is greater than 10. The relative uncertainty is only 5% when S/N is around 200. This finding is consistent with

<sup>11</sup> The uncertainties presented in Section 4.1 and Figure 3 above are different. They are based on a subset of the test sample with precise *Gaia* parallax measurements ( $\omega/\sigma_\omega > 10$ ), and are derived by comparing the predicted distances with those obtained from *Gaia* parallax.

our previous results shown in Figure 3, where we find that the scatter in the predicted absolute magnitude decreases with increasing S/N. Specifically, the median distance uncertainties for different S/N ranges are as follows: 23% for  $S/N < 20$ , 19% for  $20 \leq S/N < 60$ , 11% for  $60 \leq S/N < 100$ , and 7% for  $S/N \geq 100$ .

The bottom panel of Figure 9 shows the relative distance uncertainty as a function of distance. The distance uncertainties are obtained from the  $1-\sigma$  scatter or standard deviation of 20 Monte-Carlo samples, as detailed in Section 3.3, and we have added the 0.05 magnitudes of training uncertainty in quadrature. The uncertainty is about 14% within 2 kpc, which then quickly increases to the mean of  $\sim 50\%$  at larger distances.

#### 4.4 Distance uncertainty for giant stars and comparison with SEGUE K giants

The previous subsection (Section 4.3.2) presents the distance uncertainty statistics for all stars. In this subsection we aim to quantify the uncertainties for giant stars. We start our analysis by performing a detailed comparison with SEGUE K-giants (Xue et al. 2014).

The SEGUE distance catalog of 6,036 K-giants (Xue et al. 2014) is not based on machine learning, and instead it is a probabilistic approach under the Bayesian framework. It relies on absolute magnitude versus colour relations deduced from globular clusters with known distances and different metallicity. A median distance precision of 16% is reported. The distance catalogue can go up to 125 kpc from the Galactic center, with 283 stars beyond 50 kpc.

If we simply select giant stars with  $\log g < 3.8$ , our median distance uncertainty can be as large as 40% within 50 kpc, as quantified with the method of Section 3.3, which is significantly larger than that of Xue et al. (2014). Here our quoted 40% level of uncertainty is consistent with the left plot of Figure 6 above, where we see a scatter of about 1 magnitude (50% uncertainty in distance) based on the external validation. The major reason that our measurement uncertainty is larger than Xue et al. (2014) may be related to two factors: 1) DESI is much deeper, and thus even within 50 kpc, stars in DESI are fainter and have lower S/N in their stellar spectra; 2) difference in the methodologies adopted. If we consider a more limited sample of only stars cross matched between our catalogue and that of Xue et al. (2014), the matched stars mostly have S/N of about 20. However, the associated distance uncertainty in these matched stars is still as large as 39% based on the error estimation method of Section 3.3. The uncertainty is slightly smaller, if we quantify it using the external validation sample (see Section 2.5), but is still 34%. In addition, if we perform external validation for Xue et al. (2014), which we will discuss slightly later in this subsection, the scatter is 24%, so slightly larger than what they quoted (16%). However, our distance error for giant stars is still obviously larger than that of Xue et al. (2014) in all cases.

The key reason is very likely related to the methodology and the data set. The method of Xue et al. (2014) is dedicated to K giants, whereas our model is trained to predict the distance for a variety of different types of stars. The model that is trained to be optimized for the entire data set in our analysis, may not perform equally well as a model or method particularly aimed for giant stars. Moreover, Xue et al. (2014) adopted member stars of GCs to calibrate the relation among absolute magnitudes, colour and metallicity, whereas we only used member stars from GC for our external validation, rather than training. Lastly, stellar colours are not included in our training of this study. For our training, continuum normalized stellar spectra have to be used to ensure proper convergence in the training process. However, this causes the lose of information about the stellar

colour and effective temperature in the continuum. And most of the information in our training is from absorption lines. Further including stellar colours and photometric data in different bands may help to improve the precision in the predicted distances for giants. We will implement the above improvements in a future paper based on DESI Year-3 data.

Our quoted distance measurement above in Section 4.3.2 (with the method in Section 3.3) is only 23% for  $S/N < 20$ , but for giant stars with  $\log g < 3.8$  in our sample, we find the uncertainty can be as large as 39% at  $S/N \sim 20$  quantified by the same method. This is because, as we have checked, giant stars in our measurement have larger distance uncertainties than other stars.

Figure 12 shows the uncertainty quantified by the method of Section 3.3, versus S/N of stellar spectra, and we show this for stars with  $\log g < 3.8$  and  $\log g > 3.8$  separately. For giant stars with  $\log g < 3.8$ , we can clearly see that the uncertainties are significantly larger than those of the other stars, indicating our model predicts much larger distance uncertainties for giant stars at fixed S/N. The median distance uncertainties for giant stars with  $\log g < 3.8$  are 58% for  $S/N < 20$ , 38% for  $20 \leq S/N < 60$ , 16% for  $60 \leq S/N < 100$  and 8% for  $S/N \geq 100$ .

Despite the large uncertainties for giant stars, if we restrict our sample to stars with  $\log g < 3.8$  and with distance uncertainties smaller than 25%, we still have more than 74,000 and 1,500 stars within and beyond 50 kpc to the Galactic center, more than those in earlier surveys. This is benefited from the large DESI survey.

The top left panel of Figure 10 shows a direct comparison between our measurements and those of (Xue et al. 2014), based on a subset of matched stars. The number of matched stars is small, but the agreement is reasonable, in that the black dots go well though the red solid diagonal line, without biases. We further show in the top left panel of Figure 11 the external validation for Xue et al. (2014) based on our external validation sample (see Section 2.5). The validation looks very good, with small scatters and no particular biases. The amount of scatter based on this external validation is 24%.

#### 4.5 Comparison with other recent measurements with machine learning

In this subsection, we perform comparisons with a few other most recent and relevant spectrophotometric distance measurements, including those for LAMOST OB stars (Xiang et al. 2021), the LAMOST value-added stellar parameter catalogue (Wang et al. 2022) and the more recent measurements for DESI EDR data based on the Payne method (Zhang et al. 2024).

The methodology of our current paper largely follows<sup>12</sup> Xiang et al. (2021). The main difference is that Xiang et al. (2021) adopted stars with good parallaxes ( $\omega/\sigma_\omega > 10$ ) in their training and test samples, whereas we do not apply any cuts on parallax error; that is the main reason that we avoid biases in our distance measurements up to 100 kpc. The distance measurements by Xiang et al. (2021) focus on nearby OB stars within 15 kpc to the Sun and from LAMOST. The precision in the measured distances of Xiang et al. (2021) is claimed to be 12%. At  $S/N > 20$  and within 15 kpc, the precision of

<sup>12</sup> Note Xiang et al. (2021) also adopts PCA in their analysis. PCA has been used to remove emission lines from their OB stars.

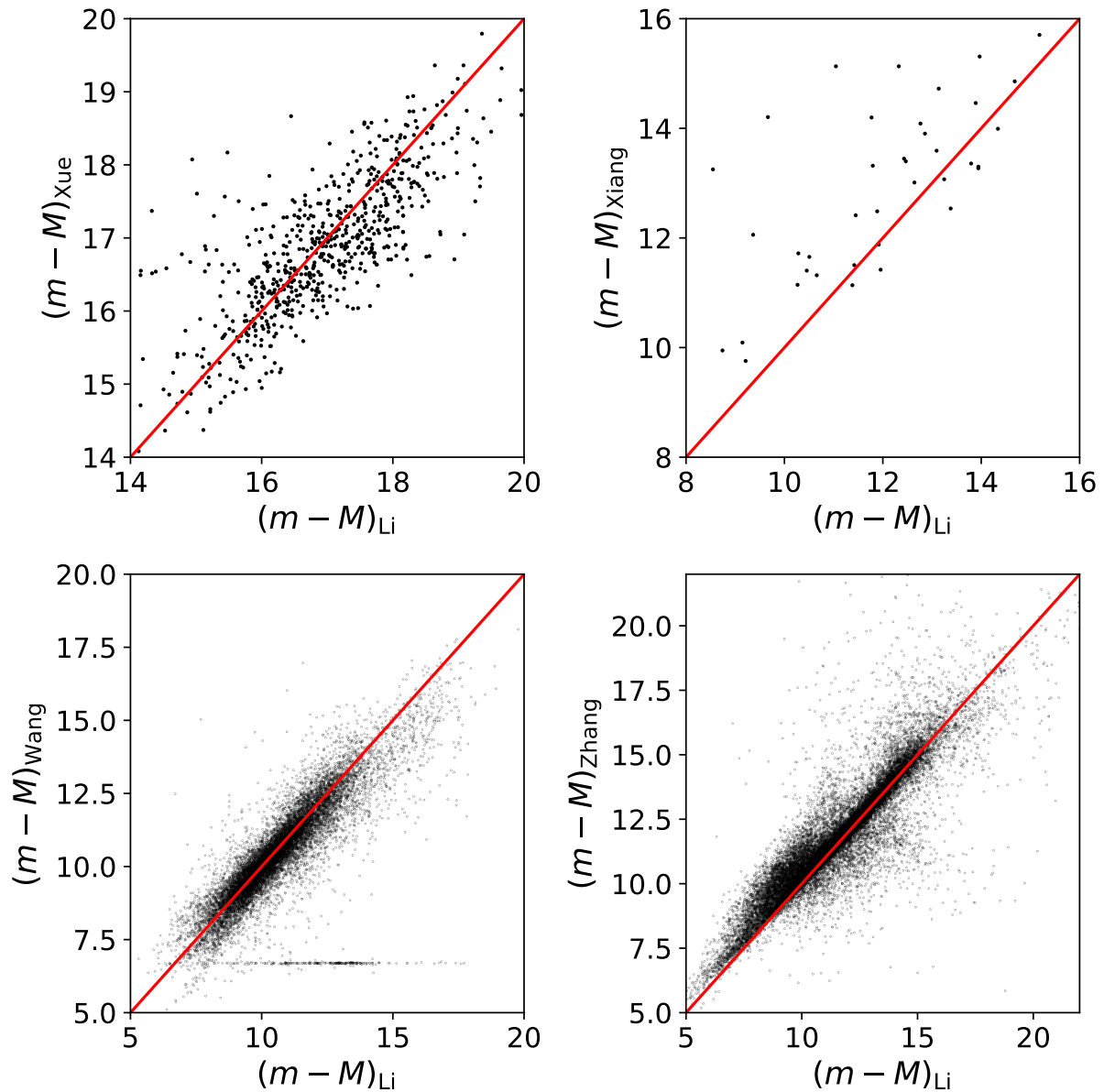


**Figure 10.** Comparison between our distance measurements in this paper ( $x$ -axis) and the spectrophotometric distance measurements in four previous studies, including SEGUE K-giants (Xue et al. 2014) (top left), LAMOST OB stars (Xiang et al. 2021) (top right), LAMOST value-added catalogue (Wang et al. 2022) (bottom left) and the more recent measurement for DESI EDR based on the Payne method (Zhang et al. 2024) (bottom right). In all panels, the red solid line marks  $y = x$  to guide the eye.

our distance measurement<sup>13</sup> is 14%, which is comparable to Xiang et al. (2021).

The more recent measurements by Wang et al. (2022) for LAMOST, and Zhang et al. (2024) for DESI EDR both cover wide stellar types, similar to ours. Both Wang et al. (2022) and Zhang et al. (2024) provide measurements of stellar parameters, with the distance measurement a by-product. Wang et al. (2022) claimed that the precision is 8.5% for  $S/N > 50$ , while our precision is 10% at  $S/N > 50$ , so the precision is comparable. However, we would like to emphasize

that the training sample of Wang et al. (2022) has only  $\sim 6,000$  stars, which is much smaller than ours. Wang et al. (2022) excluded stars with distances greater than 2 kpc (from Bailer-Jones et al. 2021), and distance relative errors greater than 15%. So their training sample is very nearby. In addition, Wang et al. (2022) limited their training sample and test sample to only stellar spectra with  $S/N > 100$ . This is very different from ours, that our precision of 10% at  $S/N > 50$  does not involve any  $S/N$  cut to the stellar spectra. We will show later in this subsection that with such a nearby and small training sample, in fact the distance measurements by Wang et al. (2022) are subject to prominent biases later in this subsection.

<sup>13</sup> (We do not limit to only OB stars here. Our distance uncertainties quoted for comparisons in this subsection are all based on the method of Section 3.3, i.e., Monte Carlos sampling of the error spectra.

The measurements of Zhang et al. (2024) were made using the data-driven Payne method (Ting et al. 2019; Xiang et al. 2019, 2022).

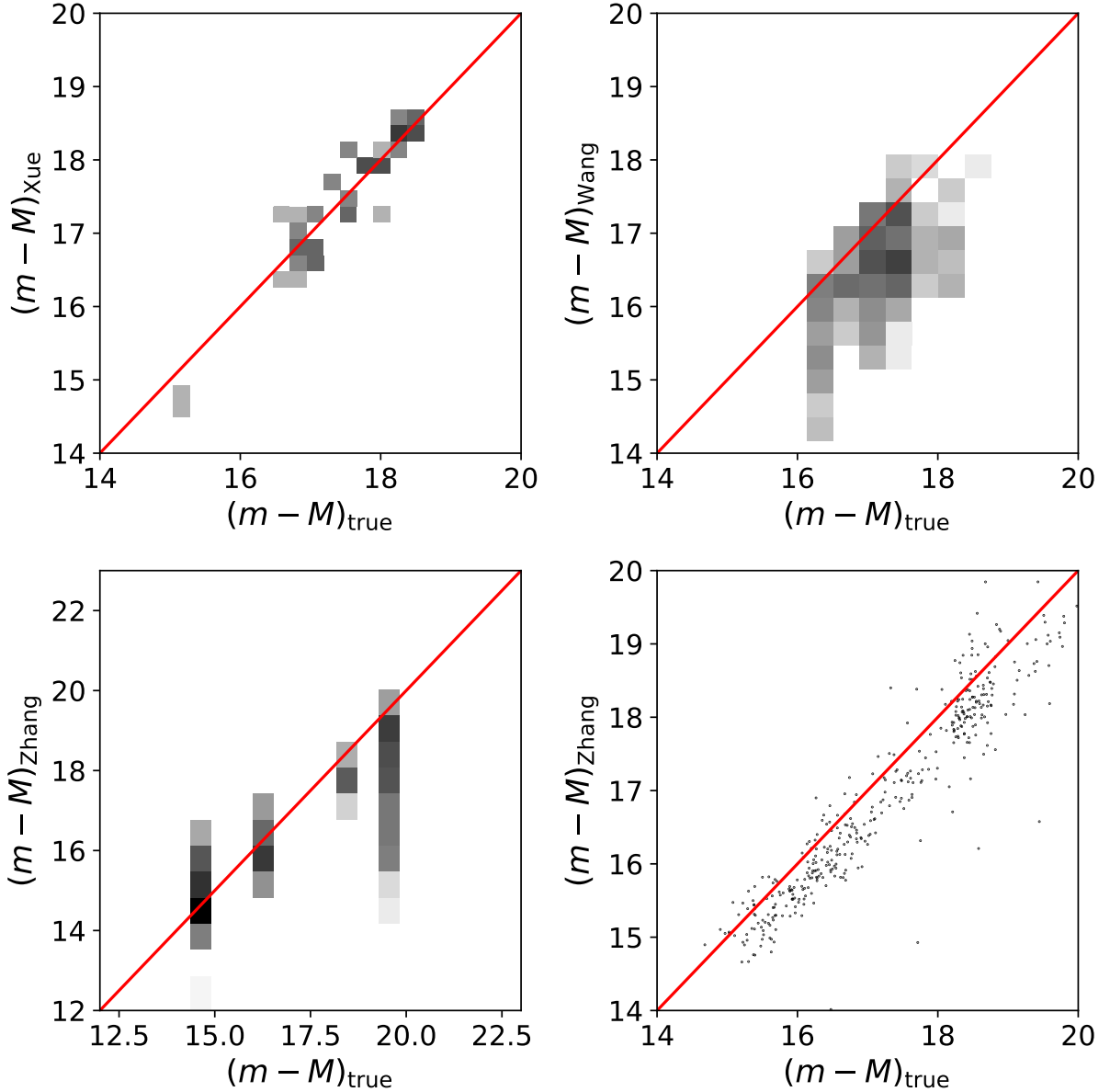


**Figure 11.** External validations for the distance measurements of (Xue et al. 2014) (top left), (Wang et al. 2022) (top right) and of (Zhang et al. 2024) (two bottom panels). For the two top panels, most stars are matched to the member star list of Sgr. The bottom left panel is based on matched member stars to a few GCs and dwarf galaxies. The right panel is based on DESI Year-1 BHB stars. The readers can check Section 2.5 about more details on the sample of stars used for external validation. In all panels, the red solid line marks  $y = x$  to guide the eye.

The Payne method is machine learning based, but instead of predicting stellar parameters from the data spectra, the model is trained to predict from stellar parameters the entire stellar spectra, and then fit to the data spectra. Their claimed precision is 14% for  $5 < S/N < 10$  and smaller than 4% for  $S/N > 50$ . Our precision is 19% for  $5 < S/N < 10$  and 10% for  $S/N > 50$ , which is less accurate compared with Zhang et al. (2024).

The top right and bottom panels of Figure 10 show direct comparisons between our distance measurements and those of Xiang et al. (2021), Wang et al. (2022) and Zhang et al. (2024), based on cross matched stars between our measurements and the public catalogues of these previous studies. The number of matched stars is small with Xiang et al. (2021), but is much larger with Wang et al. (2022) and

Zhang et al. (2024) based on the larger LAMOST and DESI EDR data sets.

In general, our measurements show reasonable agreement with all the three previous studies based on machine learning. There are, however, some detailed differences. In the top right panel, where we show the comparison with Xiang et al. (2021), the black dots tend to be more above the red diagonal line. However, this is perhaps also associated with the small sample of stars matched, so we avoid having strong comments on this. In the two bottom panels where the samples of matched stars is much larger, we can see the measured distance modulus by Wang et al. (2022) tend to fall below the diagonal line, while the measurements by Zhang et al. (2024) tend to fall above the diagonal line over distance modulus range of  $5 < (m - M)_{\text{Li}} < 12$ .

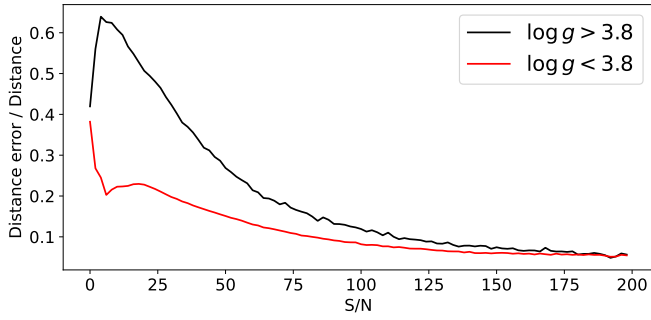


**Figure 12.** Median distance measurement errors obtained from Monte Carlo sampling the error spectra (see Section 3.3), reported as a function of the S/N of the stellar spectra. Black and red curves are for stars with  $\log g < 3.8$  and  $\log g > 3.8$ , respectively.

The bias of Wang et al. (2022) with respect to our measurements in fact becomes larger with the increase in distance. There are many fewer data points beyond distance modulus of 14, but they are mostly below the diagonal line over the distance modulus range of 14 to 18. Note that over a distance modulus range from 15 to 20, our external validation above does not show any particular bias (Figures 6 and 7). We further conduct an external validation by matching the sample of Wang et al. (2022) to the external validation set in Section 2.5. The top right panel of Figure 11 shows the results. It is clear to see that the distance measurements by Wang et al. (2022) are subject to significant underestimates, with most of the data below the diagonal line. We think the main reason behind the significantly underestimated distances is that Wang et al. (2022) used a much smaller and very nearby training sample, which has a biased parameter distribution, hence resulting in significant underestimates for more distant stars.

The two bottom panels of Figure 11 show the external validations for the distance measurements of Zhang et al. (2024). The left panel is based on member stars of a few GCs and dwarf galaxies. There is no particular bias for distance modulus of  $15 < (m - M)_{\text{true}} < 18$ , but at  $(m - M)_{\text{true}}$  close to 20 (100 kpc), there are more significant underestimates. The right panel of Figure 11 shows the validation using DESI Year-1 BHB stars. It seems there is almost a constant underestimate, while we do not see such an underestimate in our measurements (Figure 7 above).

Thus it seems our distance measurements show much less bias than those of Wang et al. (2022) and Zhang et al. (2024). This is benefited from the fact that we do not apply any parallax error and S/N cuts to our training sample, and also we have avoided excluding negative parallaxes. This avoids biasing our training sample to nearby stars. When the training sample is limited to be nearby, it may not fully cover the parameter space of more distant stars, hence resulting in significant underestimates in distances for more distant stars.

The underestimate due to the usage of biased training sample, however, cannot explain the overestimate of Zhang et al. (2024) with respect to our measurements over distance modulus range of  $5 < (m - M)_{\text{Li}} < 12$  and in the bottom right panel of Figure 10. For this overestimate, we have used a subset of stars with precise *Gaia* parallax ( $\omega/\sigma_\omega > 10$ ) to validate, and find our measurements are unbiased, in contrast to those of Zhang et al. (2024).

We do not show the validation for Xiang et al. (2021), as there are few matched stars to the external validation sample.

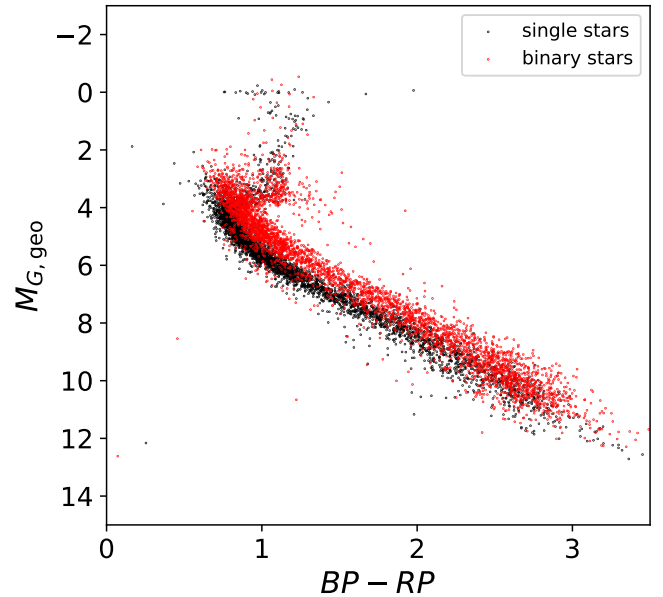


**Figure 13.** The distribution of single stars (black dots) and binaries (red dots) in Hertzsprung-Russell diagram, and binaries are identified by our Gaussian mixture model (Equation 9) with  $P_{\text{binary}} > 0.7$ . Stars plotted in the figure are based on a subset of test sample with precise parallax measurements of  $\omega/\sigma_\omega > 10$ . The  $x$ -axis is the colour index based on *Gaia* photometry in *BP* and *RP* bands. The  $y$ -axis is the geometric absolute magnitude  $M_{G,\text{geo}}$  based on *Gaia* parallax. The distribution of binaries shows a clear shift from single stars by about 0.75 magnitude.

## 5 BINARY IDENTIFICATION FROM OUR DISTANCE MEASUREMENTS

As discussed in Figure 3 above, our results are affected by the existence of binaries. Proper modeling and exclusion of binary stars in our sample can potentially enhance the precision in our distance measurements. In this section, we discuss a method of modeling and identifying binary systems. However, as we have tested, the currently proposed model is effective only for a subset of stars with small measurement errors in their parallaxes. Moreover, we expect this method to work well with main sequence binary systems of nearly equal-mass, but not for giants, whose companions are mostly dwarfs. We first introduce and discuss our proposed modeling approach below, and present some initial results at this stage.

As demonstrated in Figure 3, equal-mass binaries show an offset of about 0.75 magnitude above the diagonal line. The relationship between stellar luminosity and mass obeys a power-law form (Demircan & Kahraman 1991). If we assume that the primary and secondary stars in a binary system obey a cubic power-law relationship between luminosity and mass, the difference between  $M_{G,\text{geo,binary}}$  and  $M_{G,\text{geo,single}}$  which is also the difference between  $M_{G,\text{geo,binary}}$  and  $M_{G,\text{NN}}$  can be written as:

$$M_{G,\text{geo,single}} - M_{G,\text{geo,binary}} = 2.5(\log(1 + \rho^3)), \quad (6)$$

where  $\rho$  denotes the mass ratio of the secondary star to the primary star.

Typically,  $M_{G,\text{geo,binary}}$  is about 0.45 to 0.75 magnitudes brighter than  $M_{G,\text{NN}}$  for binary systems with a mass ratio ranging from 0.8 to 1. The differences between  $M_{G,\text{NN}}$  and  $M_{G,\text{geo}}$  of binaries are large enough to be detected by the NN, as the typical error of the NN

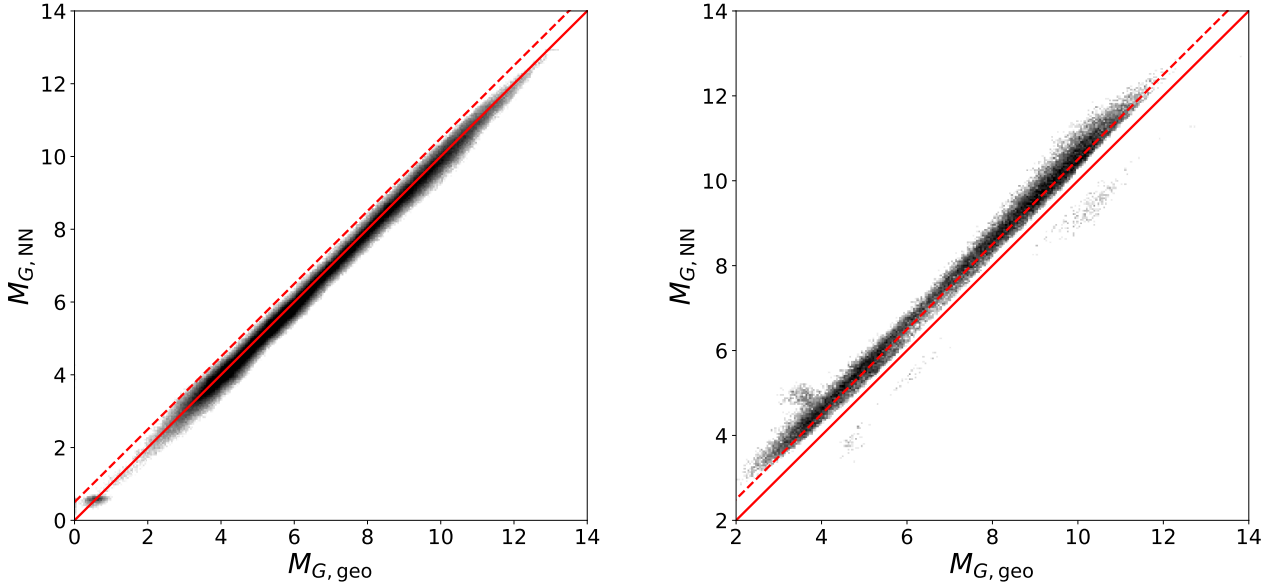


**Figure 14.** Comparison between  $M_{G,\text{NN}}$  and  $M_{G,\text{geo}}$ . Here  $M_{G,\text{NN}}$  is obtained in Section 4.1, and we only plot a subset of the test sample with precise parallax measurement  $\omega/\sigma_\omega > 10$ , based on which that we can deduce precise  $M_{G,\text{geo}}$ . We apply the method of Section 5 to distinguish binaries and single stars. The left plot is for single stars, and the right plot is for binary stars. In both panels, the red solid line shows the  $y = x$  diagonal line, and the red dash line has an offset of 0.75 magnitude above the diagonal line.

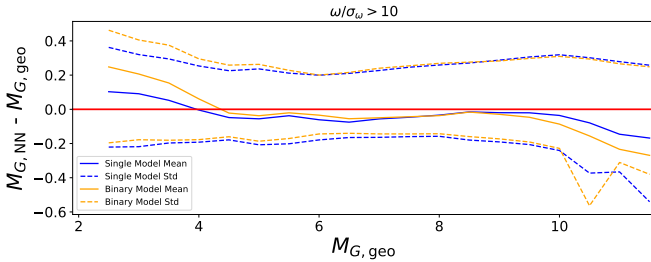


**Figure 15.** Comparison between the performance of the single star model (i.e. the model we presented in Section 4) and the binary model (i.e. the Gaussian mixture model in Section 5). The plot is based on a subset of test sample with high precision *Gaia* parallax of  $\omega/\sigma_\omega > 10$  to deduce  $M_{G,\text{geo}}$  as the reference.  $M_{G,\text{NN}} - M_{G,\text{geo}}$  is the difference between the predicted absolute magnitude and the geometric absolute magnitude from *Gaia* parallax, for the single star and binary models (see the legend). The blue and orange solid lines are the means, while the dashed lines are the associated standard deviations. The horizontal red solid line marks  $y = 0$  to guide the eye.

is much smaller than 0.45. Therefore, we can construct a new model to detect binaries.

A stellar spectrum may originate from a single star or a binary system, and thus the corresponding absolute magnitude should not be considered as a single value but rather as a distribution. We assume that the absolute magnitude obeys a Gaussian mixture distribution with two Gaussian components, with one component representing single stars and another component representing binaries. Notably, in our modeling here for binaries, we utilize absolute magnitudes as our training label. This label varies over a much smaller range than the original label we defined above.

For a given stellar observation, the Gaussian mixture model de-

scribing the distribution of absolute magnitude,  $M$ , has the following form:

$$P(M|\Theta) = \alpha N_1(M - \mu_1|\sigma_1) + (1 - \alpha)N_2(M - \mu_2|\sigma_2), \quad (7)$$

and we utilize NN to predict the five model parameters (denoted as  $\Theta = \{\alpha, \mu_1, \sigma_1, \mu_2, \sigma_2\}$ ) of the two Gaussian distributions ( $N_1$  and  $N_2$ ) for each stellar observation with standard deviations ( $\sigma_1$  and  $\sigma_2$ ), mean values ( $\mu_1$  and  $\mu_2$ ) and the fraction of each component ( $\alpha$ ). In Equation 7, the first and second Gaussian components refer to single and binary stars, respectively. Here we enforce  $\mu_1$  to be greater than  $\mu_2$  as the binary component has a brighter luminosity which leads to a smaller  $\mu$ .

The likelihood can be constructed by convolving the Gaussian mixture distribution with the observational uncertainty of absolute magnitudes:

$$\text{Likelihood} = \prod_i \int P(M|\Theta_i)P(M|\omega_{0,i}, m_{G,i})dM, \quad (8)$$

where  $P(M|\Theta_i)$  is the Gaussian mixture distribution for star  $i$ , i.e., Equation 7. The second term of  $P(M|\omega_{0,i}, m_{G,i})$  is the error model for the absolute magnitudes. Instead of assuming the error of absolute magnitude is Gaussian, we assume that the directly measured parallax error is Gaussian, and we deduce the error model for absolute magnitude from the Gaussian error of parallax as  $P(M|\omega_{0,i}, m_{G,i}) = N(10^{\left(\frac{M - m_{G,i} + 10}{5}\right)} - \omega_{0,i}|\sigma_{\omega_{0,i}})10^{\left(\frac{M - m_{G,i} + 10}{5}\right)}$ . Here  $m_{G,i}$ ,  $\omega_{0,i}$  and  $\sigma_{\omega_{0,i}}$  are the observed *Gaia*  $G$ -band apparent magnitude, parallax and parallax error for the  $i$ -th star, which are fixed values.  $i$  in Equation 8 goes for each individual star, and the parameters of the Gaussian mixture model differ for each individual star.

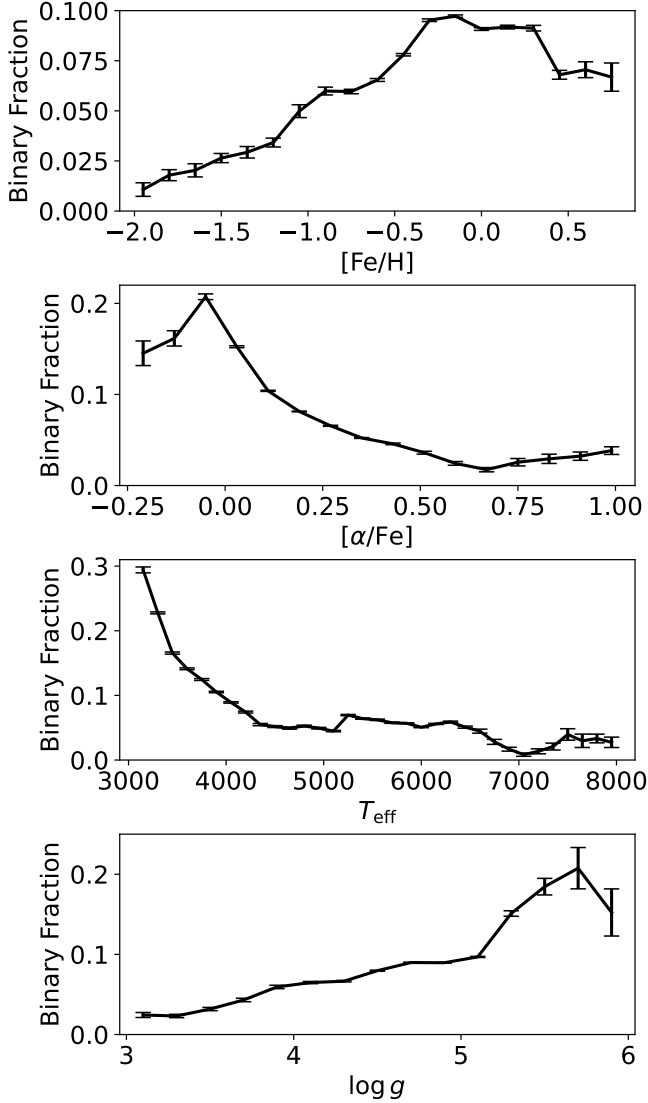


**Figure 16.** Binary fraction reported as a function of a few different stellar parameters, including [Fe/H], [alpha/Fe],  $T_{\text{eff}}$  and  $\log g$ . This is based on a subset of stars having precise *Gaia* parallax measurements, i.e.,  $\omega/\sigma_\omega > 10$ . Errorbars represent the 1- $\sigma$  scatter among 50 bootstrap subsamples.

After obtaining the best trained NN, we can estimate the probability for a given star of being a binary system as:

$$P_{\text{binary},i} = \frac{\int (1 - \alpha_i) N_2(M - \mu_{2,i} | \sigma_{2,i}) P(M | \omega_{0,i}, m_{G,i}) dM}{\int P(M | \Theta_i) P(M | \omega_{0,i}, m_{G,i}) dM}. \quad (9)$$

We apply the aforementioned modeling approach to a subset of stars with high precision parallax measurements ( $\omega/\sigma_\omega > 10$ ), and utilize Equation 9 to estimate the probability for each star to be a binary system ( $P_{\text{binary},i}$ ). Due to the relative error cuts applied to the parallax, most of the selected stars in the subsample are nearby main sequence stars located within 5 kpc. We classify a star as a binary if  $P_{\text{binary},i}$  is greater than 0.7. In this test sample, about 21,000 stars satisfy this criterion and are considered to be binaries. Figure 13 shows the distribution of these binaries identified in this way in red, and black dots are single stars. As we have already demonstrated before, the geometric absolute magnitude of binaries are greater than

single stars, that leads to a shift in HR diagram. The distribution of binaries moves upwards by about 0.75 magnitude. Figure 13 shows that our model can successfully identify binaries for the subset of stars with high precision parallax measurements.

Figure 14 compares  $M_{G,\text{geo}}$  and  $M_{G,\text{NN}}$ , and here  $M_{G,\text{NN}}$  is the NN predicted absolute magnitudes that we obtained in Section 4 (not based on the binary model in the current section). The figure is also based on the subset of stars with high precision parallax measurements. The left and right plots are for stars with  $P_{\text{binary}} \leq 0.7$  and  $P_{\text{binary}} > 0.7$ . As can be clearly seen, we are able to successfully distinguish the single and binary regions with our modeling approach, when we have precise parallax measurements.

In particular, the left panel of Figure 14 shows that the precisions in  $M_{G,\text{NN}}$  for single stars are 0.19 and 0.26 magnitudes for  $S/N > 20$  and  $S/N < 20$ , which corresponds to precisions of 9% and 13% in distance respectively. Note if not excluding binaries, the precisions in distance measurements are 10% and 18% for  $S/N > 20$  and  $S/N < 20$ .

In the right panel of Figure 14 about 10% of the identified binary stars are located below the diagonal line by a shift of about 0.5 magnitudes. These stars are distinguished and modeled by the second component of our mixture model. However, they are unlikely to be true binary systems and may instead be contaminants, such as white dwarfs. Indeed, about half of these stars do have the colours of white dwarfs. The  $S/N$  is very low for the other half, and the reason why they located below the diagonal line may be due to measurement uncertainties. In order to exclude those misclassified binary systems we further excluded those with  $M_{G,\text{NN}}$  brighter than  $M_{G,\text{geo}}$ . Our final binary criteria is:

- $P_{\text{binary}} > 0.7$
- $M_{G,\text{NN}} > M_{G,\text{geo}}$

where  $M_{G,\text{NN}}$  is from the single star model.

With our model, we can also predict the absolute magnitudes and distances. We adopt the median absolute magnitude based on the Gaussian mixture model for each DESI stellar observation. Figure 15 shows the precision in predicted absolute magnitudes for the Gaussian mixture model (the orange line, see Equation 7) and the single star model (the blue line, see Equation 4). This plot is based on a subset of test sample with high precision *Gaia* parallax of  $\omega/\sigma_\omega > 10$ . All of these stars are main sequence stars. Our Gaussian mixture model shows comparable amounts of scatters and biases than the single star model. This shows the success of both models applied to the subsample with high precision parallax measurements.

We have also applied our modeling approach of identifying binaries to the full sample of stars without cuts in parallax error. However, we find that the final converged estimates of the model parameters become unphysical when applied to the full sample. At brighter absolute magnitudes,  $\sigma_{1,2}$  can be very large, while the distances converted from  $\mu_{1,2}$  are significantly different from our distance measurements in Section 4, showing strongly biased results in the external validation. We attribute this issue primarily to the fact that giant stars dominate brighter magnitudes, and their companions are predominantly dwarfs. Consequently, our current modeling approach may not be optimal for these systems. Moreover, the parallax measurements of these more distant stars suffer from very large uncertainties at brighter absolute magnitudes (fainter apparent magnitudes as they are more distant). These large uncertainties not only hinder the ability of the model to discern a clear double Gaussian distribution, but also suggest that the error distribution of the observed *Gaia* parallaxes may not be Gaussian. We leave more detailed investigations

about how to more accurately identify binary stars and improve our distance measurements with the full sample to future studies.

With the full sample, 120,000 stars are identified as binaries with  $P_{\text{binary}} > 0.7$  and  $M_{G,\text{NN}} > M_{G,\text{geo}}$ . Among the 120,000 binary candidates, 90,000 have precise *Gaia* parallax measurements, satisfying  $\omega/\sigma_\omega > 10$ . We have checked the distribution of these 120,000 binary star candidates, and find that most of their  $M_{G,\text{NN}}$  obtained in Section 4 based on the single star model is indeed about 0.5-0.75 magnitudes fainter than  $M_{G,\text{geo}}$ , and thus we believe that the identification of these 120,000 stars as binaries is robust. In our final SPECDis VAC product (see Table 1), we include a column to indicate these 120,000 binary candidates.

Based on the identified binary stars, Figure 16 shows the dependence of binary fraction on a few different stellar parameters. Here we only present results for the subsample that has precise parallax measurements of  $\omega/\sigma_\omega > 10$ . We identify binaries with  $P_{\text{binary}} > 0.7$  and require  $M_{G,\text{geo}}$  to be fainter than  $M_{G,\text{NN}}$  of the single star model. As we have mentioned above, there are 90,000 binaries identified in this subsample, and the binary fraction is the ratio between the identified binaries versus the total number of stars in this subsample.

Figure 16 shows that the binary fraction increases with [Fe/H] and  $\log g$  and declines with  $[\alpha/\text{Fe}]$  and in  $T_{\text{eff}}$ . [Fe/H] and  $[\alpha/\text{Fe}]$  are anti-correlated, so the correlation between the binary fraction and [Fe/H] or  $[\alpha/\text{Fe}]$  is likely due to the same reason, that for stars having lower [Fe/H] (more metal poor) or higher  $[\alpha/\text{Fe}]$  (more rapid star formation), they form earlier in the Universe. Stars formed earlier have a longer time to experience possible perturbations such as close encounters with another object, resulting in disruptions of the binary systems, hence the binary fractions become lower. The explanations for the dependencies of the binary fraction on  $T_{\text{eff}}$  and  $\log g$  are less clear. It perhaps indicates that for late-type main-sequence stars, they are either born with higher binary fractions, or the binary systems evolve out the main-sequence stage earlier than those of single stars.

In the end, we emphasize that the sample of binaries we identified are mostly nearby equal-mass binaries along the main sequence, so the trends above may not be generalized to binaries with mass ratios much smaller than unity. The total binary fraction for our sample with precise *Gaia* parallax measurement ( $\omega/\sigma_\omega > 10$ ) is  $\sim 9\%$ . We leave more detailed studies on the binary fraction to future studies.

In our VAC catalogue, we also provide a column that gives the binary possibilities of stars in the full sample. However, we warn the readers that even when  $P_{\text{binary}}$  is close to unity, there can be some contamination. This happens mainly when the uncertainty of  $M_{G,\text{NN}}$  (based on the single star model) or  $M_{G,\text{geo}}$  is large. Here we recommend people to additionally include the following selection:

$$M_{G,\text{NN}} - M_{G,\text{geo}} > \sqrt{M_{G,\text{NN},\text{error}}^2 + M_{G,\text{geo},\text{error}}^2} \quad (10)$$

or simply use those stars with their  $M_{G,\text{NN}}$  fainter than  $M_{G,\text{geo}}$ .

## 6 CONCLUSIONS

In this paper, we have successfully implemented a data-driven method to estimate the spectrophotometric distances for stars from the DESI Year-1 data (SPECDis). Moreover, we have estimated distance uncertainties by Monte-Carlo sampling the stellar spectra according to the error spectra. SPECDis involves training a NN on a large sample of stars without applying selection on either *Gaia* parallax error or S/N of the stellar spectra, ensuring a broad and unbiased parallax distribution in the training sample. We have employed PCA to reduce the noise and dimensionality of the input stellar spectra, which has led to enhanced precision in distance predictions. Our NN predicts a

label constructed from the reciprocal of the square root of luminosity, which is linearly proportional to parallax, thus avoiding the need to exclude stars with negative parallaxes. Moreover, by incorporating the error in *Gaia* parallax into our loss function, we allow the NN to account for the uncertainties in parallax without biasing our training sample.

The precision in our measured distance increases with S/N for the stellar spectra. Based on Monte Carlo sampling the errors of the input spectra (see Section 3.3), we find that the median distance uncertainties for different S/N ranges are as follows: 23% for  $S/N < 20$ , 19% for  $20 \leq S/N < 60$ , 11% for  $60 \leq S/N < 100$ , and 7% for  $S/N \geq 100$ . Giant stars with  $\log g < 3.8$  are subject to much larger uncertainties of 58% for  $S/N < 20$ , 38% for  $20 \leq S/N < 60$ , 16% for  $60 \leq S/N < 100$  and 8% for  $S/N \geq 100$ . Nevertheless, after selecting giant stars with  $\log g < 3.8$  and with distance uncertainties smaller than 25%, we still have more than 74,000 and 1,500 stars within and beyond 50 kpc to the Galactic center, benefited from the large DESI survey.

External validations are also performed by using member stars from GCs, stellar streams and dwarf galaxies, which have precise distances and can be utilized as independent references. We also adopted the DESI Year-1 BHB stars for the validation. The external validation shows that there is no particular bias in our distance measurements within 100 kpc after applying an appropriate error cut.

Detailed comparisons are performed between our distance measurements and a few most relevant studies of Xue et al. (2014), Xiang et al. (2021), Wang et al. (2022) and Zhang et al. (2024). The method of Xue et al. (2014) (the SEGUE K giant catalogue) is not machine learning, and their quoted distance uncertainty is more precise than ours. The other three studies, which are all based on machine learning approaches, have similar quoted precisions as our measurements. We show in external validations that the distance measurements of Wang et al. (2022) and Zhang et al. (2024) are subject to more significant biases than ours, a result that is mainly due to their use of much smaller and more nearby training samples.

Our final SPECDis VAC product provides distance and distance uncertainty measurements for over 4 million stars, offering a valuable resource for Galactic astronomy and near-field cosmology studies. The catalogue covers a wide range of distances, with most stars located within 15 kpc from the Sun, and about 120,000 stars located beyond 15 kpc. Some stars can even extend to 250 kpc.

We have also developed a method for identifying binary systems by modeling the absolute magnitude distribution as a mixture of two Gaussian components. This approach has shown promise for a subset of stars with high precision parallax measurements, allowing us to distinguish single and binary stars, potentially improving the precision of our distance measurements and has identified 120,000 possible binaries. However, this method is currently limited to main sequence stars with precise parallaxes.

With the identified sample of binaries, we discovered that the binary fraction increases with [Fe/H] and  $\log g$  and declines with  $[\alpha/\text{Fe}]$  and  $T_{\text{eff}}$ . This likely implies that binaries that form earlier, which are hence poorer in Fe and richer in  $\alpha$ , they may have experienced more close encounters and tidal effects, hence the binary systems are disrupted more.

In summary, our work presents a robust and comprehensive distance VAC product for a large sample of stars from the DESI Year-1 data, demonstrating the power of data-driven approaches in Galactic astronomy. The catalogue will be released as one of the DESI DR1 VAC products at <https://data.desi.lbl.gov/doc/releases/dr1/vac/mws-SpecDis/>. The content and columns of our final SPECDis VAC product is provided in Table 1.

Field	Description
TARGETID	DESI source ID
SOURCE_ID	Gaia DR3 source ID
RA	Gaia DR3 Right Ascension (deg)
DEC	Gaia DR3 Declination (deg)
PMRA	Gaia DR3 Proper Motion in Right Ascension
PMRA_ERR	Uncertainty in pmra
PMDEC	Gaia DR3 Proper Motion in Declination
PMDEC_ERR	Uncertainty in pmdec
VRAD	Radial velocity (km/s)
DIST	Heliocentric distances derived from $M_{G,NN}$ (kpc)
DISTERR	Uncertainty of distance (kpc)
$M_{G,NN}$	NN predicted Gaia $G$ -band absolute magnitude
$M_{G,geo}$	Observed Gaia $G$ -band absolute magnitude derived by <i>Gaia</i> parallax
PARALLAX	Gaia DR3 parallax (mas) before zero point correction
PARALLAX_ERR	Uncertainty in parallax (mas)
PARALLAX_ZPC	Zero point correction of parallax according to Lindegren et al. (2021)
EBV	Reddening estimated in this work
A_G	Dust correction value of $M_{G,geo}$
RUWE	Gaia DR3 RUWE
APS	Gaia DR3 ASTROMETRIC_PARAMS_SOLVED
NEUIA	Gaia DR3 NU_EFF_USED_IN_ASTROMETRY
P_COLOUR	Gaia DR3 PSEUDOCOLOUR
ECL_LAT	Gaia DR3 ECL_LAT
BINARY_FLAG	Flag of binaries: 1 for single stars, 0 for binaries
BINARY_POSSIBILITY	Binary possibility of a star

**Table 1.** Contents and columns of our SPECDis VAC product for more than 4 million stars from DESI Year-1 data.

## ACKNOWLEDGEMENTS

This work is supported by NSFC (12273021,12022307) and the National Key R&D Program of China (2023YFA1605600, 2023YFA1605601). We thank the sponsorship from Yangyang Development Fund. The computations of this work are carried on the National Energy Research Scientific Computing Center (NERSC) and the Gravity supercomputer at the Department of Astronomy, Shanghai Jiao Tong University. SK acknowledges support from the Science & Technology Facilities Council (STFC) grant ST/Y001001/1. MV and YW acknowledge support from NASA ATP award (80NSSC20K0509). APC acknowledges support from the Taiwan Ministry of Education Yushan Fellowship, MOE-113-YFMS-0002-001-P2, and Taiwanese National Science and Technology Council grant 112-2112-M-007-009. HY is supported by the National Center for High-Level Talent Training in Mathematics, Physics, Chemistry, and Biology.

This study was initiated by YW and MV by training the noise free  $sp$  model spectra in the earlier Fuji internal data release of DESI, and was passed to SL and WW around the end of 2022 to continue.

We are grateful for the efforts spent on checking and coordinating our paper by the DESI publication handler, Alejandro Avilés, and by the DESI MWS working group chair, Leandro Beraldo e silva. WW is grateful for discussions with Xiaoting Fu, Maosheng Xiang, Xiangxiang Xue, Hao Tian, Jie Wang, Wenda Li, Jundan Nie, Hongliang Yan, Tian Qiu and Yanrui Zhou.

This paper is based upon work supported by the U.S. Department of Energy (DOE), Office of Science, Office of High-Energy Physics, under Contract No. DE-AC02-05CH11231, and by the National Energy Research Scientific Computing Center, a DOE Office of Science User Facility under the same contract. Additional support for DESI was provided by the U.S. National Science Foundation (NSF), Division of Astronomical Sciences under Contract No. AST-0950945 to the NSF’s National Optical-Infrared Astronomy Research Laboratory; the Science and Technology Facilities Council of the United Kingdom; the Gordon and Betty Moore Foundation; the Heising-Simons Foundation; the French Alternative Energies and Atomic Energy Commission (CEA);

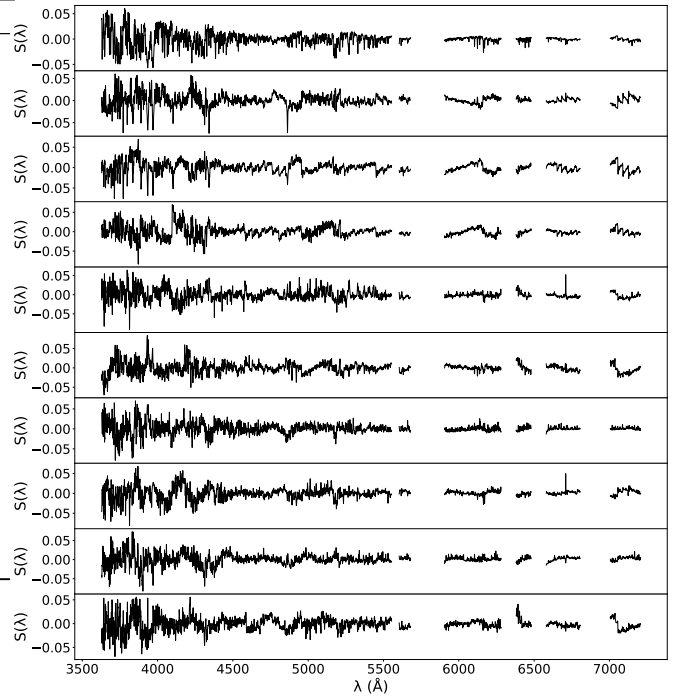


**Figure A1.** The first ten principal components of DESI Year-1 stellar spectra, corresponding to the largest ten eigenvalues. Here  $S(\lambda)$  denotes the flux of stellar spectra after subtracting the mean and after logarithmic transformation (see Equation 1). It is clear that these PCs successfully catch the line information of the stellar spectra, and contain features of cool stars. Discontinuity in the spectra is due to the masks of sky lines and bad pixels.

the National Council of Humanities, Science and Technology of Mexico (CONAHCYT); the Ministry of Science, Innovation and Universities of Spain (MICIU/AEI/10.13039/501100011033), and by the DESI Member Institutions: <https://www.desi.lbl.gov/collaborating-institutions>. Any opinions, findings, and conclusions or recommendations expressed in this material are those of the author(s) and do not necessarily reflect the views of the U. S. National Science Foundation, the U. S. Department of Energy, or any of the listed funding agencies.

The authors are honored to be permitted to conduct scientific research on Iolkam Du’ag (Kitt Peak), a mountain with particular significance to the Tohono O’odham Nation.

For the purpose of open access, the author has applied a Creative Commons Attribution (CC BY) licence to any Author Accepted Manuscript version arising from this submission.

## DATA AVAILABILITY

The measurements presented in this paper can be accessed at <https://zenodo.org/records/14903565>, which contains all data points for figures presented in this work.

## APPENDIX A: EXAMPLES OF PRINCIPAL COMPONENTS

As discussed in Section 2.4, PCA is crucial for our analysis as it captures the principal information of stellar spectra effectively, while helps to reduce the noise and dimensionality of the data spectra.

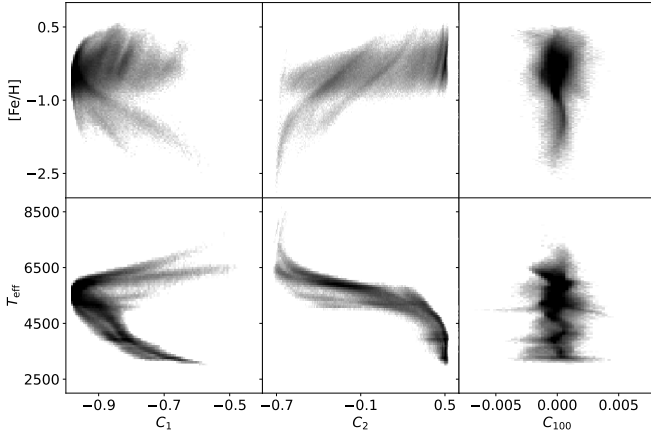


**Figure A2.** The relationships between the iron abundance,  $[\text{Fe}/\text{H}]$ , the effective temperature of stars,  $T_{\text{eff}}$ , and the coefficients of three principal components.  $C_1$ ,  $C_2$  and  $C_{100}$  represent the coefficients of the first, second and 100-th PCs. Here  $[\text{Fe}/\text{H}]$  and  $T_{\text{eff}}$  are from *rvs* table.

**Table A1.** Distance table for GCs and dwarf galaxies, the member stars of which are used for distance external validations in this paper. Here those GCs and dwarf galaxies having fewer than 10 member stars are excluded from this table.  $d_{\text{ref}}$  and  $d_{\text{NN}}$  are the reference distance and the median value of the NN predicted distances. a and b stand for reference source of (Baumgardt & Vasiliev 2021) and (Pace et al. 2022).

Name	$d_{\text{ref}}$ [kpc]	$d_{\text{NN}}$ [kpc]	References
NGC 6218	$5.109^{+0.049}_{-0.048}$	5.50	a
NGC 6205	$7.419^{+0.076}_{-0.075}$	8.99	a
NGC 5904	$7.479^{+0.060}_{-0.060}$	8.28	a
NGC 6341	$8.501^{+0.071}_{-0.070}$	9.69	a
NGC 5272	$10.175^{+0.082}_{-0.081}$	11.4	a
NGC 7078	$10.709^{+0.096}_{-0.095}$	13.4	a
NGC 7089	$11.693^{+0.115}_{-0.114}$	12.6	a
NGC 5466	$16.120^{+0.164}_{-0.162}$	15.2	a
NGC 5053	$17.537^{+0.235}_{-0.232}$	17.5	a
NGC 5024	$18.498^{+0.185}_{-0.183}$	17.9	a
Pal5	$21.941^{+0.520}_{-0.508}$	21.5	a
NGC 5634	$25.959^{+0.628}_{-0.613}$	25.0	a
NGC 2419	$88.471^{+2.437}_{-2.371}$	69.2	a
draco 1	$75.8^{+5.4}_{-5.4}$	70.1	b
sextans 1	$92.5^{+2.5}_{-2.5}$	59	b

Figure A1 presents the first ten PCs of the total sample, illustrating the significant patterns of variation within the data. We can see Balmer line features. We can also see some cool star features in the bottom panel, where there are continuous molecular absorption regions.

Figure A2 illustrates the correlation between the amplitudes of the first two PCs ( $C_1$  and  $C_2$ ) and the 100-th PC ( $C_{100}$ ) versus the iron abundance ( $[\text{Fe}/\text{H}]$ ) and effective temperatures ( $T_{\text{eff}}$ ) of the stars. The distribution of  $C_1$  and  $C_2$  indicates that the coefficients of PCs are strongly correlated with these stellar properties, suggesting that they contain physical information. The two right panels based on  $C_{100}$  show that for higher order PCs the correlations with stellar properties are significantly decreased.

However,  $C_1$  and  $C_2$  do not appear to correlate with  $[\text{Fe}/\text{H}]$  and  $T_{\text{eff}}$  linearly, and the trend is not monotonic. In the two left panels, we can see that with the increase in  $[\text{Fe}/\text{H}]$  or  $T_{\text{eff}}$ ,  $C_1$  first decreases and then increases. In addition, there are clearly sub features. This

likely reflects that  $C_1$  and  $C_2$  do not contain the information of only one stellar parameter, but can be correlated with the combinations of a few different parameters. This has been explored in, for example, a previous study of Chen et al. (2012). Understanding the physical meanings of the amplitudes for different PCs, however, is beyond the scope of this current paper.

## APPENDIX B: EXTERNAL VALIDATION OF MEMBER STARS IN GLOBULAR CLUSTERS, DWARF GALAXIES AND THE SAGITTARIUS STREAM

Figure A3 shows the external validations of our measured distances, based on the member stars of each individual GC, dwarf galaxy and the Sgr stream (see Section 2.5 for details). The green and black filled histograms show the distributions our predicted distance modulus ( $(m - M)_{\text{predict}}$ ) and the distance modulus calculated from *Gaia* parallax ( $(m - M)_{\text{geo}}$ ), respectively. The red vertical dashed line marks the reference distance of the parent GC, dwarf galaxy or stream (Baumgardt & Vasiliev 2021; Pace et al. 2022). For Sgr, we divide it into six bins according to different distance ranges and the red vertical dashed line is the mean value of distance modulus for stars in each range. It is very encouraging to see that our measured distances are approximately unbiased and show significantly smaller scatters, compared with the distances estimated from *Gaia* parallax beyond 7 kpc, when there are enough numbers of member stars in the system. The slight overestimation of NGC 6205 and NGC 5904 observed here contributes to the bias noticed in Figure 6. The blue vertical dashed line in each panel marks the median distance modulus based on our measurements. For further systems, our measurements show some under estimates, consistent with Figure 6. Note when there is a large discrepancy between the blue and red vertical dashed lines, it is mainly because the number of matched member stars is too few. We provide the reference distances and the median distance of our NN prediction, for different GCs and dwarf galaxies used for the external validation, in Table A1.

## APPENDIX C: COMPARISON BETWEEN BAILER-JONES DISTANCE AND GAIA 1/PARALLAX

Figure A4 shows the external validation of distance modulus for *Gaia* parallax and Bailer-Jones (2023) distances. It is clear that the distance modulus from Bailer-Jones (2023) is underestimated for distant halo stars. *Gaia* DR3 parallaxes, on the other hand, show very large scatter but no significant bias in the inferred distance modulus. Thus in this paper we choose to adopt the *Gaia* DR3 parallaxes for our training. In particular, since our training label is chosen as  $\omega/\sqrt{F_G}$  (Equation 3), which is linear in parallax, we expect the random scatters can cancel to large extent, with the overall prediction unbiased. If using Bailer-Jones (2023) distances, we may end up more significant underestimates for more distant stars. Note given the very large scatter in the right plot of Figure A4, it is very encouraging to see the significantly smaller scatter in Figure 6 of the main text, and the fact that our measured distances are more precise than inferred from *Gaia* parallaxes in Figure 4 of the main text and Figure A3 of the Appendix.

## REFERENCES

Allende Prieto C., Beers T. C., Wilhelm R., Newberg H. J., Rockosi C. M., Yanny B., Lee Y. S., 2006, *ApJ*, 636, 804

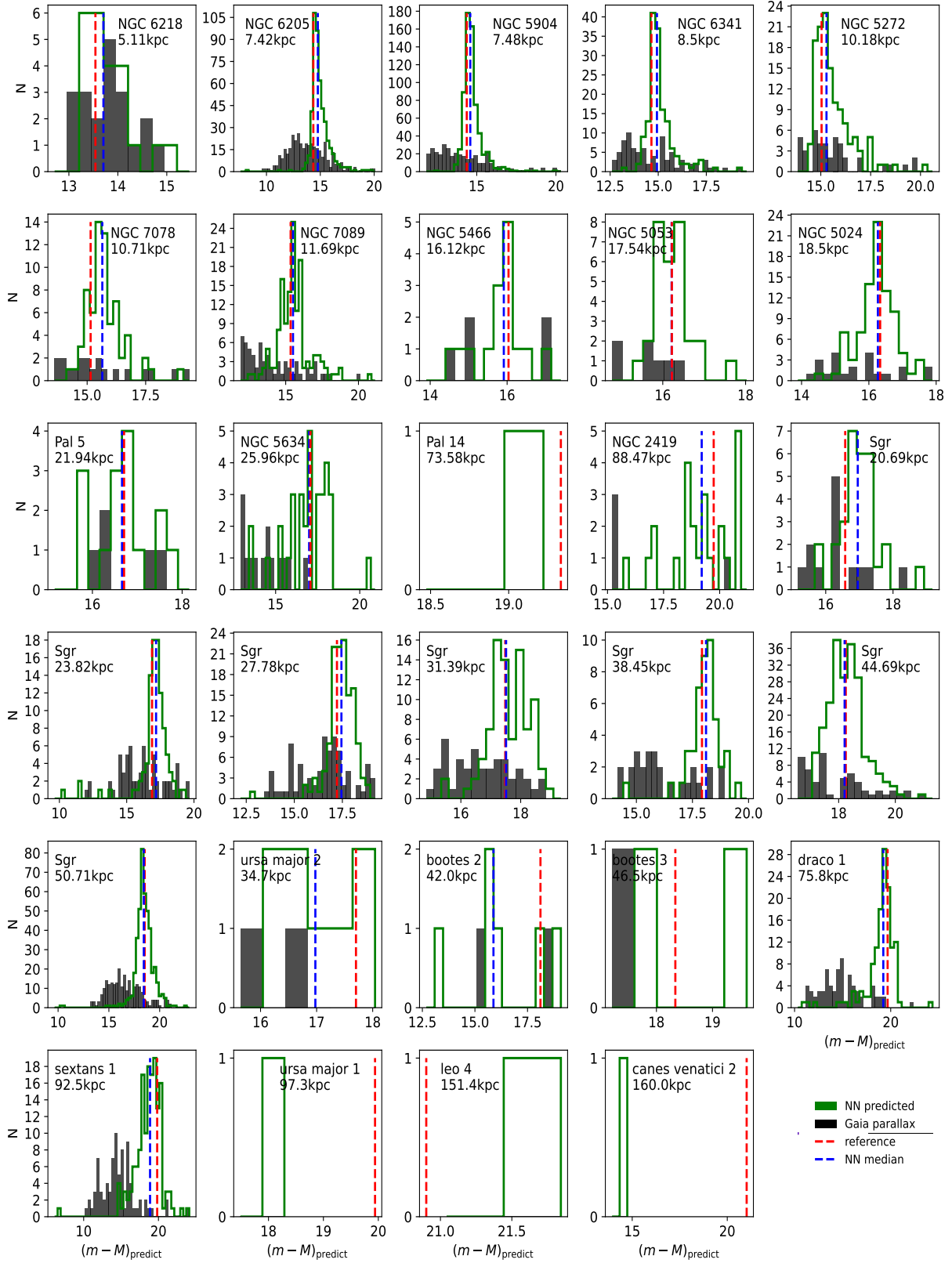


**Figure A3.** The distributions of  $(m-M)_{\text{predict}}$  predicted by NN (the green histogram) and  $(m-M)_{\text{geo}}$  derived from *Gaia* parallax (the black filled histogram). Each panel shows an individual GC, dwarf galaxy or a given distance bin of the Sagittarius stream. The red vertical dashed line marks the reference distance modulus of the parent object and the blue vertical dashed line marks the median of distance modulus predicted by NN. When the number of member stars is too few, we do not show the blue vertical line. The text in each panel indicates the name of the object and its distance.

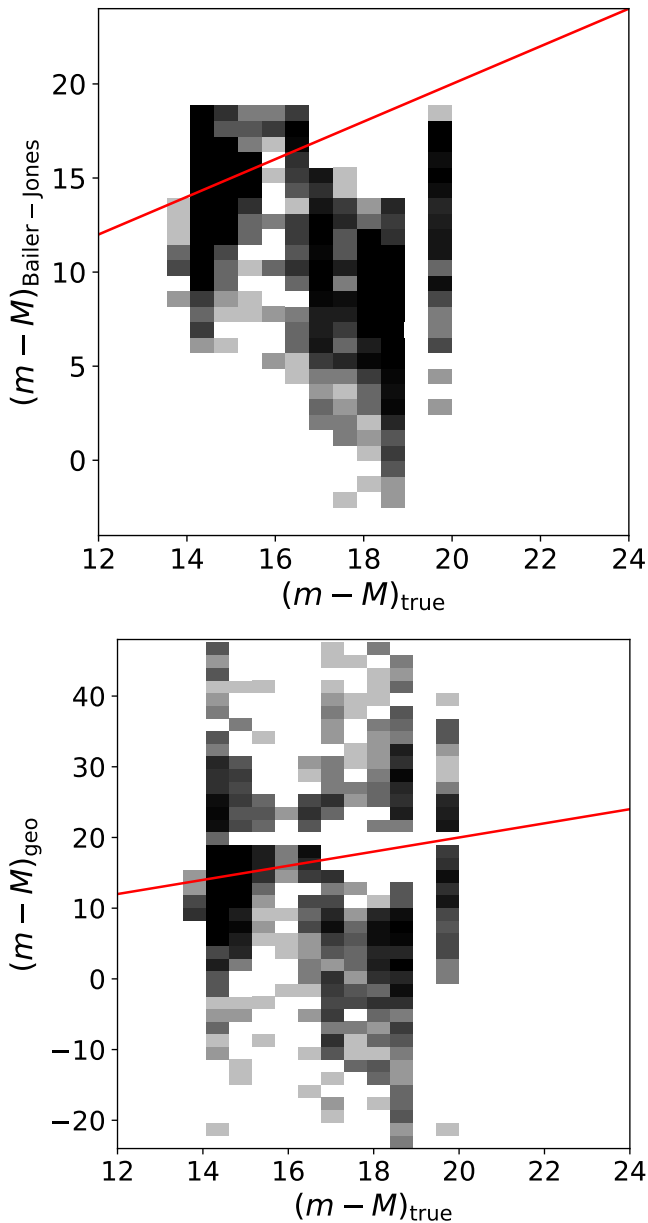


**Figure A4. Top:** Comparison between distance modulus from (Bailer-Jones 2023),  $(m - M)_{\text{Bailer-Jones}}$ , and reference distance modulus,  $(m - M)_{\text{true}}$ . **Bottom:** Comparison between distance modulus from *Gaia* parallax,  $(m - M)_{\text{geo}}$ , and  $(m - M)_{\text{true}}$ . The reference distance modulus is from GCs, Sagittarius stream and dwarf galaxy member stars which have a precise distance measurements. The red solid line marks the  $y = x$  diagonal line to guide the eye.

Bailer-Jones C. A. L., 2023, *AJ*, 166, 269

Bailer-Jones C. A. L., Rybizki J., Fouesneau M., Demleitner M., Andrae R., 2021, *The Astronomical Journal*, 161, 147

Baumgardt H., Vasiliev E., 2021, *MNRAS*, 505, 5957

Budavári T., Wild V., Szalay A. S., Dobos L., Yip C.-W., 2009, *MNRAS*, 394, 1496

Byström A., et al., 2024, *arXiv e-prints*, p. arXiv:2410.09149

Carlin J. L., et al., 2015, *AJ*, 150, 4

Chaussidon E., et al., 2023, *ApJ*, 944, 107

Chen Y.-M., et al., 2012, *MNRAS*, 421, 314

Clementini G., et al., 2019, *A&A*, 622, A60

Cooper A. P., et al., 2023, *ApJ*, 947, 37

Coronado J., Rix H.-W., Trick W. H., 2018, *MNRAS*, 481, 2970

DESI Collaboration et al., 2016a, preprint, (arXiv:1611.00036)

DESI Collaboration et al., 2016b, preprint, (arXiv:1611.00037)

DESI Collaboration et al., 2022, *arXiv e-prints*, p. arXiv:2205.10939

DESI Collaboration et al., 2024a, *arXiv e-prints*, p. arXiv:2404.03000

DESI Collaboration et al., 2024b, *arXiv e-prints*, p. arXiv:2404.03001

DESI Collaboration et al., 2024c, *arXiv e-prints*, p. arXiv:2404.03002

DESI Collaboration et al., 2024d, *arXiv e-prints*, p. arXiv:2411.12020

DESI Collaboration et al., 2024e, *arXiv e-prints*, p. arXiv:2411.12021

DESI Collaboration et al., 2024f, *arXiv e-prints*, p. arXiv:2411.12022

DESI Collaboration et al., 2024g, *AJ*, 167, 62

DESI Collaboration et al., 2024h, *AJ*, 168, 58

Das P., Sanders J. L., 2019, *MNRAS*, 484, 294

Deason A. J., Belokurov V., Evans N. W., 2011, *Monthly Notices of the Royal Astronomical Society*, 416, 2903

Demircan O., Kahraman G., 1991, *Ap&SS*, 181, 313

Dey A., et al., 2019, *AJ*, 157, 168

Gaia Collaboration Prusti T., de Bruijne J. H. J., Brown A. G. A., Vallenari A., Babusiaux C., Bailer-Jones C. A. L., Bastian U., 2016, *A&A*, 595, A1

Goodfellow I., Bengio Y., Courville A., 2016, *Deep Learning*. MIT Press

Green G. M., et al., 2021, *ApJ*, 907, 57

Guy J., et al., 2023, *AJ*, 165, 144

Hahn C., DESI Team 2022, in *APS April Meeting Abstracts*. p. H13.003

Han J. J., et al., 2022, *The Astronomical Journal*, 164, 249

Hernitschek N., et al., 2017, *ApJ*, 850, 96

Hernitschek N., et al., 2018, *The Astrophysical Journal*, 859, 31

Hogg D. W., Eilers A.-C., Rix H.-W., 2019, *AJ*, 158, 147

Huang Y., et al., 2023, *ApJ*, 957, 65

Husser T. O., Wende-von Berg S., Dreizler S., Homeier D., Reiners A., Barman T., Hauschildt P. H., 2013, *A&A*, 553, A6

Ivezić Ž., et al., 2008, *ApJ*, 684, 287

Jurić M., et al., 2008, *ApJ*, 673, 864

Koposov S. E., et al., 2011, *ApJ*, 736, 146

Koposov S. E., et al., 2024, *MNRAS*, 533, 1012

Levi M., et al., 2013, *arXiv e-prints*, p. arXiv:1308.0847

Lindgren L., et al., 2021, *A&A*, 649, A2

Miller T. N., et al., 2024, *AJ*, 168, 95

Pace A. B., Erkal D., Li T. S., 2022, *ApJ*, 940, 136

Poppett C., et al., 2024, *AJ*, 168, 245

Queiroz A. B. A., et al., 2020, *A&A*, 638, A76

Raichoor A., et al., 2023, *AJ*, 165, 126

Sartoretti P., et al., 2023, *A&A*, 674, A6

Schlafly E. F., Finkbeiner D. P., 2011, *ApJ*, 737, 103

Schlafly E. F., et al., 2023, *AJ*, 166, 259

Silber J. H., et al., 2022, *arXiv e-prints*, p. arXiv:2205.09014

Ting Y.-S., Conroy C., Rix H.-W., Cargile P., 2019, *ApJ*, 879, 69

Vasiliev E., Belokurov V., Erkal D., 2021, *MNRAS*, 501, 2279

Wang J., et al., 2016, *MNRAS*, 456, 672

Wang C., Huang Y., Yuan H., Zhang H., Xiang M., Liu X., 2022, *ApJS*, 259, 51

Watkins L. L., et al., 2009, *Monthly Notices of the Royal Astronomical Society*, 398, 1757

Xiang M. S., et al., 2017, *MNRAS*, 464, 3657

Xiang M., et al., 2019, *ApJS*, 245, 34

Xiang M., Rix H.-W., Ting Y.-S., Zari E., El-Badry K., Yuan H.-B., Cui W.-Y., 2021, *ApJS*, 253, 22

Xiang M., et al., 2022, *A&A*, 662, A66

Xue X.-X., et al., 2014, *ApJ*, 784, 170

Zhang M., et al., 2024, *ApJS*, 273, 19

Zhou R., et al., 2023a, *AJ*, 165, 58

Zhou S., Zhang P., Chen Z., 2023b, *MNRAS*, 523, 5789

<sup>1</sup> Department of Astronomy, Shanghai Jiao Tong University, Shanghai 200240, China

<sup>2</sup> Shanghai Key Laboratory for Particle Physics and Cosmology, Shanghai 200240, China

<sup>3</sup>*State Key Laboratory of Dark Matter Physics, School of Physics and Astronomy, Shanghai Jiao Tong University, Shanghai 200240, China*

<sup>4</sup>*Institute for Astronomy, University of Edinburgh, Royal Observatory, Blackford Hill, Edinburgh EH9 3HJ, UK*

<sup>5</sup>*Institute of Astronomy, University of Cambridge, Madingley Road, Cambridge CB3 0HA, UK*

<sup>6</sup>*Department of Astronomy and Astrophysics, University of Toronto, 50 St. George Street, Toronto ON, M5S 3H4, Canada*

<sup>7</sup>*Department of Physics, University of Michigan, 415 Church Street, Ann Arbor, MI 48105, USA*

<sup>8</sup>*Leinweber Center for Theoretical Physics, University of Michigan, 415 Church Street, Ann Arbor, MI 48105, USA*

<sup>9</sup>*NSF's NOIRLab, 950 N. Cherry Avenue, Tucson, AZ 85719, USA*

<sup>10</sup>*Instituto de Astrofísica de Canarias, C/ Va Lactea s/n, E-38205 La Laguna, Tenerife, Spain*

<sup>11</sup>*Universidad de La Laguna, Dpto. Astrofísica, E-38206 La Laguna, Tenerife, Spain*

<sup>12</sup>*Imperial College London, South Kensington Campus, London SW7 2AZ, UK*

<sup>13</sup>*Tsung-Dao Lee Institute, Shanghai Jiao Tong University, Shanghai 201210, China*

<sup>14</sup>*Institute of Astronomy and Department of Physics, National Tsing Hua University, 101 Kuang-Fu Rd. Sec. 2, Hsinchu 30013, Taiwan*

<sup>15</sup>*Center for Informatics and Computation in Astronomy, NTHU, 101 Kuang-Fu Rd. Sec. 2, Hsinchu 30013, Taiwan*

<sup>16</sup>*Institute for Computational Cosmology, Department of Physics, Durham University, South Road, Durham DH1 3LE, UK*

<sup>17</sup>*Lawrence Berkeley National Laboratory, 1 Cyclotron Road, Berkeley, CA 94720, USA*

<sup>18</sup>*Physics Dept., Boston University, 590 Commonwealth Avenue, Boston, MA 02215, USA*

<sup>19</sup>*Dipartimento di Fisica "Aldo Pontremoli", Università degli Studi di Milano, Via Celoria 16, I-20133 Milano, Italy*

<sup>20</sup>*INAF-Osservatorio Astronomico di Brera, Via Brera 28, 20122 Milano, Italy*

<sup>21</sup>*Department of Physics & Astronomy, University College London, Gower Street, London, WC1E 6BT, UK*

<sup>22</sup>*Instituto de Física, Universidad Nacional Autónoma de México, Circuito de la Investigación Científica, Ciudad Universitaria, Cd. de México C. P. 04510, México*

<sup>23</sup>*Department of Astronomy, San Diego State University, 5500 Campanile Drive, San Diego, CA 92182, USA*

<sup>24</sup>*NSF NOIRLab, 950 N. Cherry Ave., Tucson, AZ 85719, USA*

<sup>25</sup>*Departamento de Física, Universidad de los Andes, Cra. 1 No. 18A-10, Edificio Ip, CP 111711, Bogotá, Colombia*

<sup>26</sup>*Observatorio Astronómico, Universidad de los Andes, Cra. 1 No. 18A-10, Edificio H, CP 111711 Bogotá, Colombia*

<sup>27</sup>*Institute of Cosmology and Gravitation, University of Portsmouth, Dennis Sciama Building, Portsmouth, PO1 3FX, UK*

<sup>28</sup>*Institut d'Estudis Espacials de Catalunya (IEEC), c/ Esteve Terradas 1, Edifici RDIT, Campus PMT-UPC, 08860 Castelldefels, Spain*

<sup>29</sup>*Fermi National Accelerator Laboratory, PO Box 500, Batavia, IL 60510, USA*

<sup>30</sup>*Center for Cosmology and AstroParticle Physics, The Ohio State University, 191 West Woodruff Avenue, Columbus, OH 43210, USA*

<sup>31</sup>*Department of Physics, The Ohio State University, 191 West Woodruff Avenue, Columbus, OH 43210, USA*

<sup>32</sup>*The Ohio State University, Columbus, 43210 OH, USA*

<sup>33</sup>*Department of Physics, The University of Texas at Dallas, 800 W. Campbell Rd., Richardson, TX 75080, USA*

<sup>34</sup>*Department of Physics, Southern Methodist University, 3215 Daniel Avenue, Dallas, TX 75275, USA*

<sup>35</sup>*Sorbonne Université, CNRS/IN2P3, Laboratoire de Physique Nucléaire et de Hautes Energies (LPNHE), FR-75005 Paris, France*

<sup>36</sup>*Departament de Física, Serra Hünter, Universitat Autònoma de Barcelona, 08193 Bellaterra (Barcelona), Spain*

<sup>37</sup>*Institut de Física d'Altes Energies (IFAE), The Barcelona Institute of Science and Technology, Edifici Cn, Campus UAB, 08193, Bellaterra (Barcelona), Spain*

<sup>38</sup>*Institució Catalana de Recerca i Estudis Avançats, Passeig de Lluís Companys, 23, 08010 Barcelona, Spain*

<sup>39</sup>*Department of Physics and Astronomy, Siena College, 515 Loudon Road, Loudonville, NY 12211, USA*

<sup>40</sup>*IRFU, CEA, Université Paris-Saclay, F-91191 Gif-sur-Yvette, France*

<sup>41</sup>*Department of Physics and Astronomy, University of Waterloo, 200 University Ave W, Waterloo, ON N2L 3G1, Canada*

<sup>42</sup>*Perimeter Institute for Theoretical Physics, 31 Caroline St. North, Waterloo, ON N2L 2Y5, Canada*

<sup>43</sup>*Waterloo Centre for Astrophysics, University of Waterloo, 200 University Ave W, Waterloo, ON N2L 3G1, Canada*

<sup>44</sup>*Space Sciences Laboratory, University of California, Berkeley, 7 Gauss Way, Berkeley, CA 94720, USA*

<sup>45</sup>*University of California, Berkeley, 110 Sproul Hall #5800 Berkeley, CA 94720, USA*

<sup>46</sup>*Instituto de Astrofísica de Andalucía (CSIC), Glorieta de la Astronomía, s/n, E-18008 Granada, Spain*

<sup>47</sup>*Departament de Física, EEBE, Universitat Politècnica de Catalunya, c/Eduard Maristany 10, 08930 Barcelona, Spain*

<sup>48</sup>*Department of Physics and Astronomy, Sejong University, 209 Neungdong-ro, Gwangjin-gu, Seoul 05006, Republic of Korea*

<sup>49</sup>*CIEMAT, Avenida Complutense 40, E-28040 Madrid, Spain*

<sup>50</sup>*University of Michigan, 500 S. State Street, Ann Arbor, MI 48109, USA*

<sup>51</sup>*Department of Physics & Astronomy, Ohio University, 139 University Terrace, Athens, OH 45701, USA*

<sup>52</sup>*National Astronomical Observatories, Chinese Academy of Sciences, A20 Datun Rd., Chaoyang District, Beijing, 100012, P.R. China*

This paper has been typeset from a  $\text{\TeX}/\text{\LaTeX}$  file prepared by the author.